SANDIA REPORT
SAND2024-11111
Printed Click to enter a date

Sandia National Laboratories

In situ Characterization of Soot Aggregates Produced by Burning Contaminated Liquid Fuels with Nuclear Waste Surrogate

Raiya Ebini, Joshua A. Hubbard, Christopher M. Sorensen, Dora K. Wiemann, Taylor Settecerri, Alex Brown

Prepared by
Sandia National Laboratories
Albuquerque, New Mexico
87185 and Livermore,
California 94550

Issued by Sandia National Laboratories, operated for the United States Department of Energy by National Technology & Engineering Solutions of Sandia, LLC.

Available to DOE and DOE contractors from
U.S. Department of Energy
Office of Scientific and Technical Information
P.O. Box 62
Oak Ridge, TN 37831

Telephone: (865) 576-8401
Facsimile: (865) 576-5728
E-Mail: reports@osti.gov
Online ordering: http://www.osti.gov/scitech

Available to the public from
U.S. Department of Commerce
National Technical Information Service
5301 Shawnee Rd
Alexandria, VA 22312

Telephone: (800) 553-6847
Facsimile: (703) 605-6900
E-Mail: orders@ntis.gov
Online order: https://classic.ntis.gov/help/order-methods/

ABSTRACT

The motivation of this work was to complement other studies intended to enhance and update DOE-HDBK-3010-94 for hazard scenarios like nuclear waste fires. The contaminants (e.g., actinides) released during a fire, within the soot matrix, need to be investigated and characterized. The size of these contaminated soot particles and related morphology are important factors in respiratory health assessments. In this work, a uniquely designed combustion chamber was successfully integrated with a light scattering technique to characterize soot aggregates. The chamber design allowed for soot investigation within the flame as well as after soot left the incandescent flame region. While the soot aggregates were about 0.5 μm in size within the incandescent part of the flame, the aggregates in the smoke outside the flame were an order of magnitude bigger in size (5.0 μm). Variations in the experimental setup caused some variation in the size and morphology of the detected soot aggregates. This work demonstrates the use of light scattering for in-situ characterization of soot aggregates in nuclear waste fires and lays the foundation for additional work characterizing soot size and morphology.

CONTENTS

LIST OF FIGURES

LIST OF TABLES

EXECUTIVE SUMMARY

Respirable fraction is defined in DOE-HDBK-3010-94 [1]as the fraction of airborne radionuclides that can penetrate the respiratory system. Hence, it is an important factor in health assessments. Usually, airborne particles of 10 μm or less are considered respirable. The DOE-HDBK-3010-94 provides a collection of experimental data and analysis from which airborne release fraction and respirable fraction may be derived. This information is important in determining the quantities of airborne radioactive material for estimating potential hazards associated with such a release, and the consequences to humans and the environment. This information aids in making vital health assessments. Data in the handbook are more than 40 years old. Experiments and data analysis can be updated with state-of-the-art aerosol measurements and techniques. Hubbard et al. [2], [3] worked on quantifying the airborne release fraction of nuclear waste surrogates in an attempt to repeat experiments documented in DOE-HDBK-3010-94. They found that the mass of the contaminants released was not directly proportional to the mass of the material consumed by fire[2], [3]. Following the efforts of Hubbard et al., this work aims to provide a real time picture of airborne soot and its growth. Ultimately, this picture helps determine whether the soot particles are respirable or not. In addition, this work aims to provide further understanding of the distribution of contaminants within the aerosol population. This work, combined with previous studies, guide in health assessment updates for DOE-HDBK-3010-94.

In a fire, small (few tens of nanometers) soot particles are formed. If the fire occurs under-ventilated conditions, the soot particles will have the chance to collide. After collision the attractive van der Waals forces will make them stick together forming aggregates [4], [5]. These aggregates have many voids in their structure and are known as fractal aggregates. The mass of a fractal aggregate scales with its size to a power that is smaller than the spatial dimension. This power is called the fractal dimension. The fractal dimension quantifies the morphology of an aggregate. The higher the fractal dimension, the denser the aggregate. The soot aggregation mechanism follows diffusion limited cluster-cluster aggregation which yields aggregates with a fractal dimension of 1.7 – 1.8 [5], [6], [7]. Soot aggregates commonly form via the diffusion limited cluster-cluster aggregation mechanism and have a fractal dimension of 1.7 – 1.8. However, in some cases, compaction may occur due to shear [8], [9], [10], [11] or surface coating [12], [13]. In both cases, the compacted fractals have a fractal dimension up to 2.5. Additionally, soot aggregates may form hybrid structures[14], [15], [16] where at relatively short length scales (about 1μm) the aggregates have a fractal dimension of 1.8, but larger structure aggregates (about 10μm) have a fractal dimension of 2.5. This hybrid structure is known as a super-aggregate structure, and it usually occurs for sooty fuels [14].

Light scattering is a non-invasive technique used to probe soot aggregates. In a light scattering experiment the light enters the scattering system, e.g. an aerosol of soot particles, with a direction called the incident wave vector. The scattered light leaves the system with a direction called the scattering wave vector. The angle between these two vectors is called the scattering angle. The scattering is elastic, hence, these vectors have the same magnitude, and that magnitude is $2\pi/\lambda$, where λ is the wavelength of light. The detected scattered light depends on the magnitude of the vector difference between the incident and scattered wave vectors known as the scattering wave vector q. This wave vector has an inverse length unit and is a function of the scattering angle which is easily controlled during the experiment. Then by changing the scattering angle the light probes different length scales of the scattering particles; hence, the structure of the particles including size is measured.

In practice, when the scattered light is plotted against the wave vector, on a log-log scale, the size and morphology of the aggregates are uncovered [17], [18].

In this work, a uniquely designed combustion chamber [2] was integrated into a light scattering setup to characterize soot aggregates produced from liquid fuel fires contaminated with nuclear waste surrogates. Three sets of experimental variations were explored.

- For the first experimental variation, the chamber was not used. Instead, the laser beam passed through the smoke generated from a simple table-top wick burner. The laser beam passed through the smoke 130 mm above the wick burner while the smoke exiting a funnel. The laser beam intersection with the smoke defined the scattering volume. The fuels selected for this configuration were kerosene and toluene. Kerosene aggregates were about 7 μm in radius with a fractal dimension of 1.7 ± 0.05. Toluene, which is a sootier fuel, produced super-aggregates of 7 μm with hybrid morphology of 2.6 ± 0.1 and 1.7 ± 0.05 [14].
- For the second experimental variation, a 75mm diameter glass dish was used for the open pool fire of kerosene that was ignited inside the chamber, but the soot particles travelled about 3 meters from the flame before entering a glass chromatography tube. The scattering volume was inside the glass tube. The detected signal indicated aggregates of about 7.5 μm in radius with a fractal dimension of 1.6 ± 0.1. Soot produced in the flame, within the incandescent flaming region, were small aggregates of about 0.5 μm. When these small aggregates traveled the 3-meter distance they had more residence time to aggregate and grow before they reach the scattering volume [5]. This resulted in bigger soot aggregates 3 meters downstream of the flame. Modest soot deposition was observed on the glass tube during this experiment. As a result, a nitrogen purged glass tube was designed to be implemented in future experiments to eliminate soot deposition onto the glass. In this study, both the flame and the smoke experienced shear forces created by the air flow within the chamber and tubing. We hypothesize that shear forces did affect soot characteristics and recommend additional investigation.
- The third experimental variation included two burning mechanisms inside the chamber: a 10 mL wick lamp and an open pool fire. The laser beam again passed through the luminous flame inside the chamber.
    - For the 10 mL wick lamp, aggregates formed inside the chamber from burning kerosene and toluene. The kerosene light scattering signal revealed small aggregates with 0.6 μm radius. In contrast, the signal from burning toluene showed an order of magnitude bigger aggregates with dense structures of 2.5 ± 0.1 in fractal dimension. These dense structures might be due to either shear [8], [9], [10], [11] or surface coating effects [12], [13]. The chamber design allowed for varying the blower speed. Blower speed influenced aggregate characteristics. For example, higher blower speeds produced bigger aggregates.
    - Open pool fires with liquid kerosene and kerosene-based mixtures were used in this study to complement and mimic the airborne release fraction study done by Hubbard et al.[2]. Like the work in Hubbard et al., three fuels were used: (1) kerosene, (2) kerosene and tributyl-phosphate, and (3) kerosene, tributyl-phosphate, and Ytterbium nitrate. Light scattering signals were measured for different blower speeds. Blower speed appeared to influence aggregate size while in the incandescent portion of the flame. This is consistent with the 10 mL wick lamp experiments. Additionally, a subtle

feature in the collected signal, at higher speeds, was observed for the fuel type contaminated with nuclear surrogate (Yb nitrate). This observation was subtle and should be scrutinized through additional experiments with different metals (i.e., Lu and 238-U). If similar scattering patterns are observed for other metals, this may provide an exploitable signature of fires containing metals within the carbon soot.

This work showed that different experimental variations including blower speed led to different results in the light scattering signal. Additionally, this work demonstrates the viability of using an in-situ light scattering technique to study soot aggregates while in the flame and in the smoke downstream of the incandescent region of the fire. To the best of our knowledge, this may be the first-time soot in the incandescent region of the fire, and downstream of that region, have been studied. In the final year of the project, we will make additional measurements to elucidate soot formation and growth in the absence and presence of metal contaminants which serve as surrogates for nuclear materials like uranium and plutonium.

ACRONYMS AND TERMS

Acronym/Term	Definition
ADLS	Angle dependent light scattering
ARF	Airborne release fraction
DLCA	Diffusion limited cluster-cluster aggregation
HEPA	High efficiency particulate air [filter]
HTP	Hydrogenated tetrapropylene
K/TBP	tributyl phosphate in kerosene
LII	Laser-induced incandescence
OFP	Open pool fire
PDA	Photo-diode array [detector]
RF	Respiratory fraction
RLCA	Reaction limited cluster-cluster aggregation
SASLS	Small angle static light scattering
SEM	Scanning electron microscopy
SV	Scattering volume
TBP	Tributyl-phosphate
STEM	Scanning transmission electron microscopy
TSI	Threshold sooting index
WALS	Wide-angle light scattering
RDG	Rayleigh-Debye-Gans

1. INTRODUCTION

Under incomplete combustion, hydro-carbon fuel fires produce soot. Soot is an airborne contaminant creating adverse effects on human health and the environment. If the fuel is contaminated with hazardous material, like an actinide, the aerosols produced signify a health risk if respirable [19]. There is a lack of knowledge on the composition of individual carbon/actinide particles in nuclear waste fires. Such knowledge is important to assess the exposure of the workers during the fire itself, as well as post fire investigations [20], [21]. Additional knowledge would facilitate estimating the toxicological impact of such events [22], [23]. Thus, in this study we place emphasis on understanding the chemistry and physics of airborne contaminant particles.

Due to the inherent hazards associated with actual nuclear waste, surrogates for the nuclear waste are involved in basic laboratory studies [24], [2], [3]. Ouf et al. [24] used cerium and ruthenium as surrogates for hazardous materials dissolved in a mixture of organic solvents like tributyl phosphate (TBP) and hydrogenated tetrapropylene (HTP). They reported higher airborne release fractions (ARFs) for ruthenium in comparison with cerium. They related this finding to increased volatility of ruthenium under fire conditions. Additionally, they reported an aqueous nitric acid phase formed under the contaminated solvent. Boiling of this phase enhanced the release of contaminant material. They concluded, "Bubble bursting is the main driving mechanism explaining the airborne release of nonvolatile contaminants during this type of hazardous scenario." Additionally, Ouf et al. conducted a comprehensive literature review. The summary included a wide range of studies using different liquid fuel types, contaminants, and pool sizes and the reported average of ARF in each study. An interesting observation they made is that pool size had little influence on the aerosol release fraction.

Hubbard et al. [2] studied the ARF from small fires contaminated with depleted uranium and lanthanide nitrates as nuclear waste surrogates in a mixture of 30% tributyl phosphate in kerosene (K/TBP). The lanthanide species used were lutetium and ytterbium. The objective of their work was to target the data reported in DOE-HDBK-3010-94 [1], [25], which outlines the ARFs of nuclear waste contaminants in a fire from liquid fuel like K/TBP. The data reported in DOE-HDBK-3010-94 is more than 40 years old. The goal was to reproduce these experiments using state-of-the-art aerosol measurements and instrumentation to enhance the understanding of particulate formation and transport from fires containing nuclear waste. Such understanding can develop additional basis for updating and refining nuclear facilities rules and regulations for nuclear safety assessments. In that study, a uniquely designed combustion chamber was used to capture particulate from small fires containing nuclear waste or nuclear waste surrogates, thereby enabling more accurate quantification of ARFs. The chamber's inner surface was constructed from porous material to allow for combustion air to be brought in uniformly around the fire and direct the combustion product away from chamber walls and up to an aerosol collection filter. Details of chamber design, fluid, and fire dynamics were discussed in Hubbard et al. paper. The soot collected from the aerosol filter was used for scanning electron and scanning transmission electron microscopies (SEM) and (STEM), respectively. SEM images showed aggregates of primary particles up to 60 nm in diameter and occasionally revealed 200 nm spheroid particles dispersed within the soot aggregate matrix. STEM was used to analyze the composition of the 200 nm spheroids to confirm they were composed of lanthanide (lutetium or ytterbium) phosphates. The average ARFs and standard deviations for depleted uranium were 1.0×10^{-3} and 7.5×10^{-4} respectively, consistent with the data provided by the DOE-HDBK-3010-94, which gave a range between 2×10^{-4} to 3×10^{-3} for uranium ARFs. The average ARFs for lutetium and ytterbium were about two orders of magnitude less than the depleted uranium. They proposed that ARF might be dependent on the solubility of the metal nitrate in the K/TBP and that the metal nitrate solubility might differ according to the elemental composition and temperature. Additionally, their

study showed that 25% of the total sample mass was lost whereas 0.1% of the critical contaminant (e.g., depleted uranium) was lost, representing several orders of magnitude difference. In other words, the mass of contaminants released is not necessarily directly proportional to the mass of material consumed by fire. They hypothesized that gelation and precipitation might impact the release of metal contaminants.

In an additional effort to provide more scientific information for nuclear safety assessments, Hubbard et al. [3] conducted experiments aimed at reproducing the data presented in DOE-HDBK-3010 for burning solids contaminated with nuclear waste. For this purpose, a standard method for doping cellulosic matrix was developed using Whatman-41 cellulose filters. These filters were shredded using a common office shredder. The matrix was then placed in a glass petri dish and doped with either metal nitrate in solution or mesoparticles of metallic salts. The metals used were lutetium, ytterbium, and depleted uranium. The petri dish with the doped material was placed in the combustion chamber discussed in Ref. [3], where the solids were ignited, and fiber glass filters were used to capture the aerosol particles. The filter was leached, and the leachate was analyzed. It was found that the cellulosic mass loss was approximately 10% higher for the lanthanide mesoparticles relative to the lanthanide nitrates. The ARFs were 1×10^{-4} for the nitrates with 10% uncertainty, and 3×10^{-3} for the metallic mesoparticles with 30% uncertainty. Even though the ARFs were consistent across the two metals, there was an order of magnitude difference with respect to mesoparticle salt versus nitrate solution. Additionally, the mass release of the contaminant material and the cellulosic material was found not to be directly proportional to each other. This is consistent with their finding in Ref [3].

Generally, respirable fraction (RF) can be defined as the fraction of inhaled airborne particles that can penetrate the respiratory system. RF is widely adapted in health assessments due to the health hazards associated with airborne released particles [19], [26], [27], [28], [29], [30], [31], [32]. It was found that the penetration depth and deposition rate of airborne particles in the respiratory tract generally increase as the particle diameter decreases [30], [32]. During nasal inhalation, the nasal cavity's cilia and mucus effectively filter particles larger than 10μm. These larger particulates predominantly settle in the upper respiratory tract, such as the nose and pharynx. Once inhaled, mechanisms like sneezing and coughing expel them [30]. On the other hand, particles with diameters below 10 μm are considered especially detrimental to health due to their ability to penetrate deeply into the respiratory tract, reaching the alveoli and potentially affecting the lower respiratory system [31]. The presence of RF can compromise respiratory health, increasing the risk of diseases like pneumonia and asthma. Because of individual biological variability in respiratory health status, breathing patterns (rate and route), in addition to variability in airway structures as well as gender and age, it is hard to have an agreement on the size of these particles and the depth of penetration within the respiratory track among different health assessment agencies. In this report, the definition of RF will be adapted from DOE-HDBK-3010-94 as follows: "The fraction of airborne radionuclides as particles that can be transported through air and inhaled into the human respiratory system and is commonly assumed to include particles 10 μm Aerodynamic Equivalent Diameter (AED) and less." Note that RF generally relates to any type of airborne particles. DOE-HDBK-3010-94 focuses on the hazards of airborne particles associated with radioactive metals that exhibit additional hazard to the human health and environment due to radiation. For example, enrichment of ^{235}U is accomplished by separating ^{238}U, which has a low radiation hazard because of its long half-life, but it is still an alpha emitter with high ionization capacity. Its radiotoxic risk is enhanced by its decay into other isotopes [19], [33]. Uranium and its salts are highly toxic as they may cause serious health issues like subtle changes in the genome of the cell, even short exposure can cause cancer, dermatitis, renal damage, and acute arterial lesions [33].

In Hubbard et al. [2], [3] the unique chamber design allowed for filter collections to perform ARF, SEM, and TEM analysis. Hubbard et al. provided some information regarding the contaminants released within the soot matrix, however, reaching a full picture was not provided since ARF filter analyses were destructive.

To complement previous studies, this work aims to perform in-situ characterization of soot and soot contaminated with surrogates of nuclear waste by using non-invasive, angle dependent light scattering (ADLS) techniques. ADLS techniques can provide information about the sample in real-time without the need for destructive analysis or sample extraction. For example, the size and morphology can be measured for the newly produced hot soot within the flames as well as the more mature cooled soot making up the smoke. That is because soot particles agglomerate and form bigger size structures with possibly different morphologies[5], [14], [34], [35]. In-situ characterization can provide a real time picture of the airborne soot particles and their growth mechanism to determine whether they are within the RF cut-off size or not. Additionally, it can provide a whole picture of the distribution of the contaminants within the aerosol population. This information will further support health assessment updates for DOE-HDBK-3010-94.

Key takeaways:

- Previous Airborne Release Fraction (ARF) studies showed that the mass of metallic contaminants released is not directly proportional to the mass of the material consumed by fire.
- Respirable Fraction (RF) defines the aerosols that can penetrate the respiratory system and it is important in health assessments. Usually, airborne particles of 10 μm or less are considered respirable.
- This work aims to:
  - provide a real time picture of airborne soot and its growth to facilitate whether particles are respirable or not, and
  - develop additional understanding of the distribution of contaminants within the aerosol population which will, combined with previous studies, guide in health assessments.

1.1. Theory

This section presents theoretical background on

- soot formation and aggregation, and
- light scattering theory.

1.1.1. Soot Formation and Aggregation

The formation of soot in hydrocarbon flames has many universal features that are explained in Shaddix and Williams [4]. When a flame is ignited, the heat breaks apart the hydrocarbon chains, making up the fuel material, in a process called pyrolysis. Radicals are produced along with gases like acetylene (C_2H_2). Some of these radicals react with each other to form rings of carbon that will keep growing to eventually form the black carbon particles giving up H_2 gas in the process. These molecules will aggregate together to form soot aggregates. As the soot aggregates move up the flame, they react with oxygen molecules, and may break apart. Hot particles incandesce, creating the flame's bright yellow glow. If soot formation occurs in under-ventilated conditions, soot particles will further aggregate and leave the flame as smoke. Forrest and Witten [36] were the first to show that these soot aggregates

have a fractal morphology with a characteristic fractal dimension, D_f. Hence, they are fractal aggregates.

Fractals are common in nature: trees, lightening, seashells, circularity systems in animals and even galaxies have fractal character [37]. Fractals have repeating branching morphologies from which scale invariance develops. As an example, break off a branch of a tree, and put it in the ground and you will have a miniature tree. In other words, the part looks like the whole; thus, trees are scale invariant. Another consequence of the repeating branching nature of fractals is that their mass scaling dimension is a fraction of the spatial dimension (d=3), and thus is called the fractal dimension D_f. Hence the name fractals for soot aggregates.

Generally, if small particles are allowed to stick together, they may form ramified fractal aggregates. Soot initially forms as individual spherical particles. In under-ventilated conditions, soot particles quickly become an aggregate structure made up of large number of these primary particles. These primary particles are called monomers. This is shown in the SEM image in Figure 1 taken from the previous works of Hubbard et al. These soot aggregates were produced from an open pool fire of kerosene.

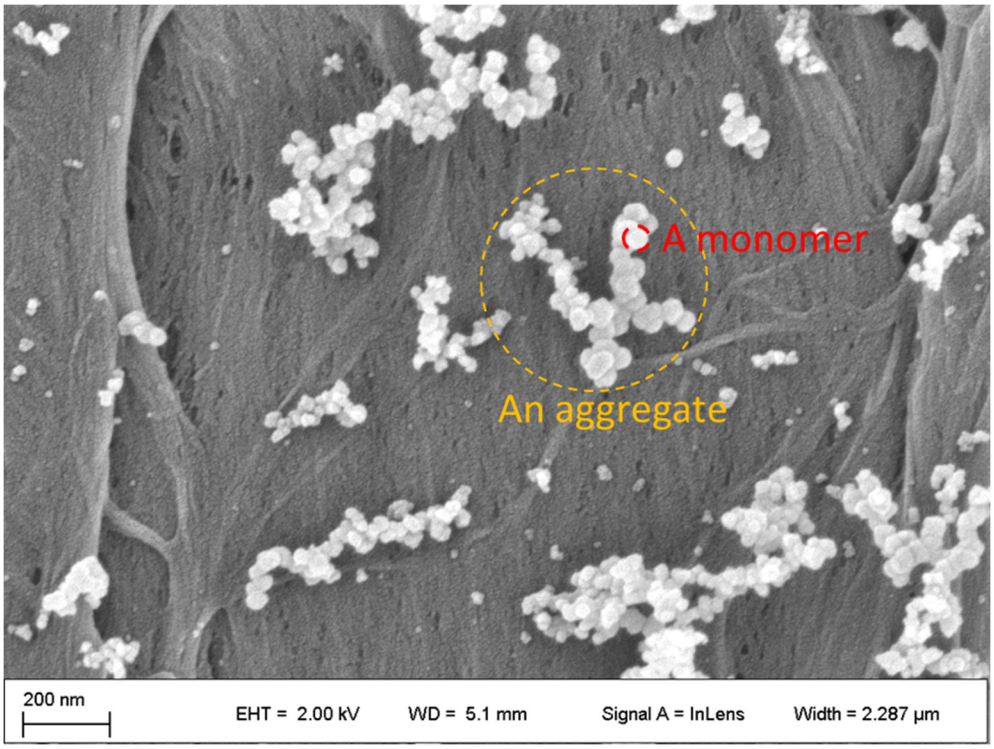

Figure 1. SEM image of soot aggregates generated from open pool kerosene fire.

Fractal aggregates are self-similar over a particular range because they are made of finite sized monomers (few tens of nanometers) and can grow up to a certain size (up to sub-millimeters). The mass of these aggregates is described by the number of monomers (N) in the aggregate. The mass scales with its size, represented by the radius of gyration, R_g, as:

$$N = k_0 \left(\frac{R_g}{a}\right)^{D_f} \quad (1)$$

where k_0 is the scaling prefactor and a is the monomer radius [5].

These aggregates have a porous structure because $D_f < d\ (= 3)$. To picture this, let us assume the total volume of the material, $V_{Tot.mat}$, makes up the soot aggregate is equal to the number of monomers N multiplied by the volume of each monomer v , $V_{tot.mat} = Nv$. Since $N \sim R_g^{D_f}$, then, $V_{Tot.mat} \sim R_g^{D_f}$. However, the fractal aggregate volume $V_{F.agg}$, scales with its own radius as $V_{F.agg} \sim R_g^3$, which is greater than $V_{Tot.mat}$. Qualitatively, the smaller D_f , the larger size this aggregate can become without needing much constituent material. The result is a more porous aggregate. D_f represents the morphology of these aggregates.

Fractal aggregates may form via two limiting regimes, diffusion limited and reaction limited cluster-cluster aggregation, DLCA and RLCA, respectively [38]. If the monomers stick together after only a single collision, due to the unshielded attractive van der Waals forces, and both monomers and aggregates are exhibiting diffusive motion, then the aggregates are formed in the DLCA limit [5], [38], [39]. The resulting aggregates will have a fractal dimension ranges between 1.7 - 1.8 [6], [7], [40]. This D_f value represents an open structure. On the other hand, if the van der Waals forces are partially shielded due to the presence of repulsive forces, the monomers will need to collide many times before they stick. Under this set of conditions, the aggregate is formed in the RLCA limit with a fractal dimension of about 2.15 [7], [40], [41]. In the RLCA limit, monomers stick together with much lower probability, allowing them to penetrate further within the aggregate body resulting in denser fractal morphology represented in higher D_f.

It is a common practice in literature to model soot aggregates via the DLCA limit [42], [43], [44]. This is because many experimental evidences support this model for soot aggregates formation [5], [17], [43]. Nevertheless, nascent soot particles may rebound after collisions due to higher mobility and lower potential well depths compared to mature soot [45]. Numerical simulations were performed to explore the aggregation of soot particles formed in a laminar premixed flame [46]. The goal was to investigate the transition from RLCA to DLCA for soot particles. It was found that the sticking probability tends to become unity in a very short period, on the order of a few milliseconds and that soot particles indeed, form aggregates via DLCA [46].

Key takeaways:

- Initially, soot primary particles are formed (tens of nanometers) but they soon they form fractal aggregates, with fractal mass to size scaling.
- Many soot aggregates form via diffusion limited cluster-cluster aggregation (DLCA) with a fractal dimension of 1.8.
- Fractal dimension determines the morphology of an aggregate. The higher fractal dimension, denser the aggregate.

1.1.2. Light Scattering Theory

The foundation of light scattering is in the phase relations of the waves scattered from the different volume elements within scattering objects. The phase relation between the incident wave and the scattered wave, that reaches the detector at position $\vec{R}$, is defined by the position of the scattering element, $\vec{r}$, and the vector $\vec{q} = \overrightarrow{k_i} - \overrightarrow{k_s}$. Here, $\vec{q}$ is the scattering wave vector and $\overrightarrow{k_i}$ and $\overrightarrow{k_s}$ are the

incident and scattered wave vectors, respectively. This is shown in Figure 2. The magnitude of q is given by [17]:

$$q = \frac{4\pi}{\lambda} \sin(\frac{\theta}{2}) \quad (2)$$

where λ is the wavelength and θ is the scattering angle. The wave vector q has units of m^{-1}, q^{-1} therefore represents the length scale of the scattering experiment[17].

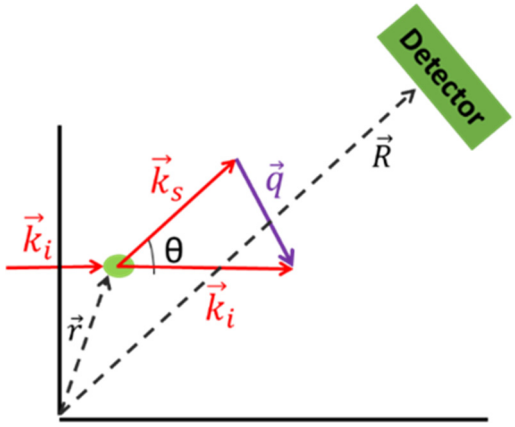

Figure 2. A classical picture of light incident from left with wave vector $\vec{k_i}$ scattering from a scattering element positioned at $\vec{r}$ toward the detector with scattering wave vector $\vec{k_s}$ at scattering angle θ. Diagram also shows the scattering wave vector $\vec{q} = \vec{k_i} - \vec{k_s}$.

Light scattering from soot aggregates can be described by the Rayleigh-Debye-Gans (RDG) theory for fractal aggregates[17], [47]. RDG theory assumes that each point in the scatterer is unaffected by the other and the light collected at the detector is due to a single scattering, hence, scattered only once (i.e., no multiple scattering) [17]. The scattered light from a fractal aggregate depends on the number of monomers in the system and to a stronger degree on the aggregate size. A log-log plot of I(q) vs. q, where I(q) is the light scattered off the particle, will have some distinct features.

The first feature is called the Rayleigh regime where I(q) is independent of θ (and hence is q independent) and can be written as I(0) or I_o. The Rayleigh regime lies in the region $qR_g < 1$ and ends near $qR_g \simeq 1$ ($\theta \approx \lambda/2\pi R_g$). Hence, for small particles this regime will extend further in q space.

The Rayleigh regime is followed by the Guinier regime at $qR_g \simeq 1$. Guinier's analysis of scattering data allows for determining the radius of gyration, R_g, of any arbitrarily shaped particles and is applicable for $qR_g \simeq 1$. For fractal aggregates, the size of the aggregate is the q^{-1} value, from the scattering intensity graph in a double logarithmic scale, that corresponds to I(q) = (2/3) I(0).

The third regime is the power law regime where I(q) is strongly dependent on q. In this regime the morphology of the system can be deduced depending on the slope (the q exponent). For a fractal aggregate of radius R_g, consisting of N spherical monomers of radius a, the log-log plot of I (q) vs. q will provide a power law regime for the aggregate. The power law regime can be expressed as $I(q) \sim q^{-D_f}$ where the exponent is D_f, revealing the aggregate's morphology. This is shown in black in Figure 3 where the slope is -1.8 for a typical DLCA aggregate. For monomers, the power law regime will appear at higher q and can be expressed as: $I(q) \sim q^{-(d+1)} \sim q^{-4}$ with a spatial dimension d=3 [17], [40], [47], [48]. This regime is shown in blue in Figure 3.

Generally, the smallest size ADLS techniques may detect is determined by the wavelength of light used in the experiment. If visible light is used, then the monomers will often go undetected as they are tens of nanometers in size, an order of magnitude smaller than the visible light wavelength.

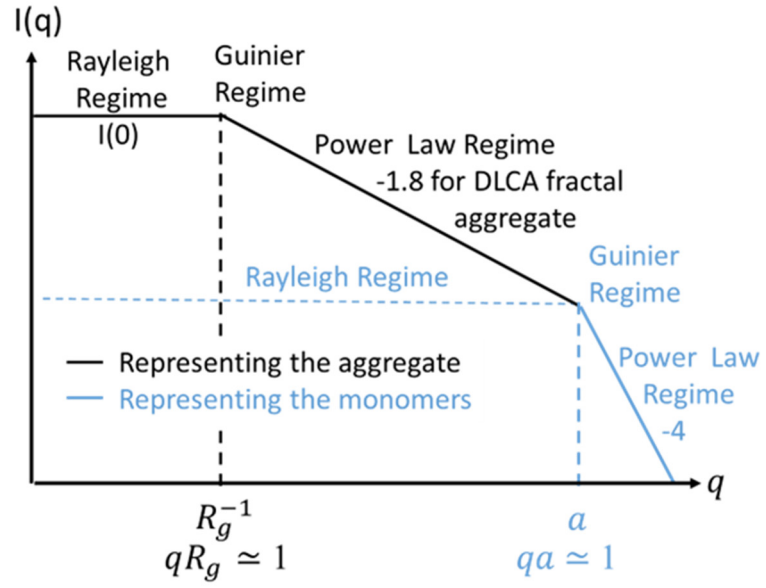

Figure 3. A schematic diagram of the scattered intensity from a DLCA fractal aggregate of radius R_g and fractal dimension D_f made up of spherical monomers of radius a, with a spatial dimension d = 3. Black represents aggregate and blue represents spherical monomers.

Key takeaways:

- Scattered light plotted on a log-log scale can provide the size and morphology of the scatterer.
- The inverse of the scattered wave vector q^{-1} represents the length scale of the system.

1.2. Further Comments on Aggregation Morphology and Soot Studies

1.2.1. Further Comments on Aggregation Morphology

Previous sections discussed the application of light scattering theory to analyze soot aggregation. Soot aggregation often proceeds via the DLCA limit with a fractal dimension of 1.8. However, the literature shows that in certain situations different morphologies have been observed. This section summarizes these conditions and findings.

Some studies showed fractal aggregates restructuring to form compact aggregates due to a coating mechanism [12], [49], [50]. These dense aggregates have fractal dimensions up to about 2.5 [12], [13]. Colbeck et al. [12] studied morphological changes of soot aggregates when exposed to high humidity ranges from 97% to 103% where 103% represents supersaturation of water vapor. They subjected the smoke to compression/expansion cycles to reach the desired saturation ratio. The goal was to model the cloud processing of smoke that might occur in the atmosphere. Sixty nanometer diameter soot particles were generated by combustion of liquefied petroleum gas (primarily butane) in air. The soot particles were left to age through further Brownian coagulation for 4 hours. The fractal dimension for the aged aggregates was found to be 1.78. The aged aggregates were then exposed to different levels of humidity. They found that increasing the relative humidity leads to a collapse of the aggregates to denser fractals with fractal dimension up to 2.5 for 103% relative humidity. Corbin et al. [50]

investigated the effect of surface coating on the aggregate's compaction. They produced soot using a quenched propane diffusion flame. The soot aged to reach a mature mobility diameter of 300 nm before using a custom coating apparatus to add a surface coating of oleic acid. They found that soot aggregates coated in combustion systems or in the atmosphere are expected to become compacted due to the coating process. Mikhailov et al. [13] worked on the restructuring mechanisms of soot particles in the presence of condensed vapor. Soot was produced using petroleum, wood, and natural gas. Vapor condensation on to the surface of previously rarefied soot aggregates led to the formation of compact fragments of close packed globules. The effect of water vapor depends on the charge and chemical composition of the particles making up the aggregates. The presence of water vapor increased the fractal dimension and shifted the size distribution toward smaller particles [13]. They proposed that the soot aggregates adsorbed water acting as condensation nuclei, and fractal restructuring occurred due to the significant effect of surface tension.

Other studies showed that compaction of fractal aggregates may occur as a function of impact velocity or shear [8], [9], [10], [11], [51], [52], [53]. Rothenbacher et al. [8] studied the mechanical stability of diesel aerosol generated by an idling diesel engine. The authors determined fragmentation probabilities of individual agglomerates versus impact velocity. The experimental set up was designed to fragment particles directly from the aerosol phase. After these aerosols were aged, they were passed through a thermo-denuder to remove adsorbates at 280°C prior to aging in some experiments. In others, it was not passed through the thermo-denuder. It was found that the energy needed for agglomerate fragmentation for dried and aged soot was less than the energy needed to fragment aerosols that contained adsorbates. Regardless of whether the aerosol particles were dried or not, aggregates exhibited a higher degree of fragmentation with increased impact velocity. Even though the authors did not measure the fractal dimension, the aggregate morphology can be seen in Figure 4 of their paper where the morphology of ramified structure at low velocities transform to a more globular structure at higher velocities. Additionally, many colloidal aggregate studies show that compact aggregates can be formed by shear-induced fragmentation [9], [10], [51], [52], [53]. In those studies, compaction resulted in a fractal dimension increase from 1.8 for DLCA aggregates to higher values of approximately 2.5 [9], [10], [11].

Additionally, hybrid slopes in the fractal power law regime with about have been observed. The -2.6 slope was pushed toward smaller q values hence larger aggregates sizes [11], [14], [15], [54], [55], [56]. This was first observed by Kim et al. [14]. They studied soot aggregates in an acetylene/air laminar diffusion flame at different heights from the burner using small angle light scattering. Their light scattering data revealed that there was a distinct change in the aggregate's morphology with increasing distance from the burner. At the highest distances, a hybrid aggregate structure with two fractal dimensions of 1.8 and 2.6 was discovered. Greater distances corresponded to late aggregation times, hence more chance for the aggregating system to develop and grow. They proposed that this hybrid structure was an indication of super-aggregates. The term super-aggregates comes from the fact that a big aggregate is composed of smaller aggregates. At large length scales these super-aggregates have a $D_f \simeq 2.5$ to 2.6 and are composed of smaller aggregates with $D_f = 1.8$ at smaller length scales. The super-aggregates appear with fuels of large sooting indices, i.e., heavily sooting flames [15]. Additionally, they occur when the aggregates are in the dense regime [5], [15], [16], [42] defined as when the nearest neighbor separation is less than 10 times the aggregate size [5], [40]. Super-aggregates have been observed in different situations involving dense aerosols, such as a turbulent fuel pool fire [54], a forest fire[55], and inverted flames[56]. This hybrid structure was also observed in colloidal shear flows [11].

Key takeaways:

- The compaction of soot fractal aggregates may occur when particle surfaces are coated by condensed species, or due to fluid shear. In both cases the compact fractals yield fractal dimensions (D_f) up to 2.5.
- Hybrid structures of soot aggregates have been observed and referred to as super-aggregates with $D_f \simeq 2.5$ and 1.8.

1.2.2. Further Comments on Soot Studies

ADLS techniques are widely used for soot diagnostic and characterization. The essence of these techniques relies on the light scattered off individual particles. Another common light measurement technique used for soot diagnostics is laser-induced incandescence (LII) [49], [54], [57], [58], [59]. This technique depends on light absorption by soot rather than scattering [49], [57], [60]. In LII, absorbing particles get heated by the laser, followed by subsequent photodetection of the radiative emission from the particles [49], [57].

Most of the applications of LII were performed on incandescent soot while in the flame. Desgroux et al. [61] investigated the soot formation in a low-pressure (from 20 to 28 KPa) flat flame using LII. The laminar premixed flames of methane/oxygen/nitrogen were stabilized on a McKenna burner. The low-pressure flames made it possible to examine early steps of soot formation. In this study they kept the equivalence ratio constant but changed the pressure. It was found that soot volume fraction increased after a given distance above the burner. Additionally, they observed that the volume fraction followed a power law dependence on the pressure. Mounton et al. [58] presented their work on the formation of soot particles in low-pressure premixed $CH_4/O_2/N_2$ flames using LII. In this study they stabilized the pressure at 26.6 kPa but used different equivalence ratios. The LII response to laser fluence has been measured for different equivalence ratios at different height above the burner in the flames. They found that soot particle growth increased when using higher equivalence ratios as well as with increasing the height above the burner. Kearny and Pierce [60] presented the use of LII and SEM imaging techniques to large scale turbulent pool fire testing. The 2m diameter pool fire blended toluene and methanol liquid fuels with 10% and 30% toluene. The LII images revealed soot structures in submillimeter size ranges, whereas SEM images showed structures ranged from 10 - 100 μm. Analysis of the SEM images reveals super-aggregate structures with D_f of 2.5-2.6 at 10 μm length scale and D_f of 1.8 at 1-2 μm length scale. These observations were dominant using 30% toluene in the blend sample. Additionally, LII enabled the measurement of the particle volume fraction with higher accuracy than using extractive sampling techniques.

Other studies combined the use of LII and ADLS techniques. Langenkamp et al. [59] combined the two techniques to investigate the soot volume fraction and aggregate size in 1D premixed C_2H_4/air flames as a function of height above the burner. Soot was produced in the flames at atmospheric pressure using a McKenna burner. They used the LII technique to measure soot volume fractions and the ADLS technique to measure the corresponding aggregate size. The flame temperatures were varied by changing the exit velocity of the unburnt gas mixture. It was found that the soot volume fraction and radius of gyration strongly increase in richer flames. Furthermore, both showed a nonmonotonic dependence on flame temperature. Soot volume fraction reached its maximum value at ~1675 K and radius of gyration was maximum at ~1700 K.

ADLS techniques have been used to characterize soot aggregates in the flame. Oltmann et al. [62] provided a design for a wide-angle light scattering (WALS) technique to characterize soot and aggregate morphologies in combustion using a continuous laser. A key feature of their design is using an ellipsoidal mirror which is used to collect scattered light with a 10^o – 170^o angular range. They

performed measurements for various sooting flames produced by premixed combustion in flat flame McKenna burner. In this work the laser passes through the flame itself where they measured primary soot particles of 50 - 90 nm for ethene, and soot aggregates of 260 nm for ethyne. The latter had a fractal dimension of 1.7. The same group extended the use of their WALS to apply it for a weakly turbulent flame [63]. For this purpose, they used a pulsed laser to carry out measurements faster than the characteristic time scale of the unsteady, turbulent system under study. To test the use of a pulsed laser, they reapplied the technique to the laminar premixed flat flame burner. The data exhibited good agreement with averaged data in their previous work [62]. The authors then applied the technique to measure the aggregate sizes in a weakly turbulent diffusion jet-flame, which was made of equimolar mixture of ethyne/nitrogen. The light scattering findings were verified by data obtained from TEM analysis of sampled soot.

Gangopadhyay et al. [64] studied the flame from methane and oxygen premixed gasses at different heights from the burner. The flame was supported on a cooled porous frit burner. The burner was surrounded by an annular sheath region of nitrogen. This arrangement yielded a one-dimensional flame. They used a static light scattering technique and found that aggregate sizes increased with increasing height in the flame. Aggregates were found to have $D_f \approx 1.8$. Additionally, Kim et al. [14] used small angle light scattering to investigate laminar diffusion flames in ambient air at different heights from the burner. Three types of fuel were used: gaseous, liquid, and solid fuels. They observed super-aggregate structures regardless of the fuel type. These structures were appeared at larger heights in diffusion flames for fuels with high sooting tendency. The same group extended their investigation of the super-aggregate formation at different heights in the flame combining small and wide-angle light scattering techniques. In this study they were able to provide a physical explanation of the super-aggregates appearance. At low heights in the flame, DLCA aggregates with D_f=1.8 are small and far apart from each other. Higher in the flame, the aggregates have more time to grow resulting in larger aggregates. They are in closer proximity and start forming super-aggregates which, if allowed, eventually will began touching and form a gel-like network. This is true for fuel with threshold sooting index (TSI) larger than 10 [15].

Soot aggregates leaving the flame and making up the smoke were also investigated. Lee et al. [65] performed a study on the flame structure and soot characteristics for a small kerosene pool fire. The burner consisted of coaxial pans for liquid fuel and water. The liquid fuel pan diameter ranged from 15 to 60 mm. Fuel pan diameter was used to vary heat release rates. The water pan was introduced to prevent overheating. Both water and fuel were connected to reservoirs to maintain constant liquid levels. Light extinction measurements were performed on the smoke to measure the soot volume fraction. Morphological characterization of the soot was performed by thermophoretic sampling with a TEM grid. It was found that flame height increased with increasing fuel pan diameter and flickering decreased. In a turbulent flame, smoke density increased with heat release rate. The TEM images revealed more mature soot particles produced with the wider fuel pan.

Chakrabarty et al. [66] used a large angle light scattering setup to study soot aggregation produced from a reversed gravity (up-side-down) laminar methane/air diffusion flame. In this study they observed the super-aggregate morphology even in their low-sooting flame. Gautam and Sorensen [67] combined small, wide-angle light scattering, and back scattering techniques, to study aerosols. Gautam discussed in his dissertation [68] his effort to generate soot with two methods: one using a lab-made premixed burner and the other using a commercially available miniature inverted soot generator. The soot from the premixed burner was produced by burning a mixture of ethylene (C_2H_4) and propane (C_3H_8) with oxygen, whereas the soot from the inverted soot-generator was obtained burning ethylene in air. They found that morphology and soot size distribution depended on the time interval between

soot generation and light scattering measurements. In both cases they witnessed enhanced back scattering. Enhanced back scattering was also observed in a separate C_2H_4/C_3H_8 premixed flame [69].

This study presents in-situ characterization of the size and morphology of the incandescent soot aggregates, while in the flame, as well as the cooled soot aggregates after they left the flame as smoke. While in the flame, soot particles might form small aggregates. This is because they only have short lifetime over which to coagulate. Aggregates in the smoke have longer times to grow resulting in bigger aggregates, which may also introduce morphological changes. Laser diagnostic techniques are heavily described in the literature as being used to study soot and soot aggregates. ADLS and LII techniques are commonly used in soot studies. In principle, these techniques rely on either light scattering off the particles or light absorption by the particles. Most of the studies in the literature focus on the study of soot while in the flame using the LII technique and to lesser extent on studying the soot after it leaves the flame as smoke. This work applies ADLS, specifically, a small angle light scattering technique, to the soot both in the flame as well as in the smoke. Additionally, the previous section gave multiple examples of aggregate morphology deviating from the standard DLCA (1.8 fractal dimension). These changes can be a caused by shear, surface coatings, or even system development into a dense aggregate with the appearance of the super-aggregates. These changes will yield different morphologies and sizes. For example, shear and coating effects might lead to small compact aggregates. In the atmosphere, wind can create shear forces and humidity can condense onto the particle. These effects might result in aggregate compaction. The impact of these changes can be of unique importance to specify the RF. Hence have a vital role in health assessments in these hazardous scenarios.

Key takeaways:

- Laser diagnostics appear widely in the literature. The two main concepts are either light scattering (i.e., ADLS) or light absorption and subsequent incandescence (i.e., LII).
- Most of the studies in the literature were performed on soot in the flame, and to a lesser extent, on the soot after it leaves the flame.
- The current work is unique because we study soot aggregates in flame, and after they leave the flame as smoke, with light scattering.
- In the future, additional parameters may be studied. How do humidity and shear affect aggregate size and morphology? These phenomena could impact the respirable fraction of particles emitted from nuclear waste fires.

2. EXPERIMENTAL DESIGN AND PREPARATIONS

This section discusses the following topics.

- Optical design
- Experimental variations
  - Burning and scattering volume outside the chamber
  - Burning inside the chamber but scattering volume outside the chamber
  - Burning and scattering volume inside the chamber
- Setup calibration
- Preparing the surrogate waste

2.1. Optical Design

Figure 4 shows a schematic diagram of the experimental light scattering apparatus. A vertically polarized laser beam of λ=532nm in *vacuo* (Laserglow, model R533001GX) was passed through the sample. The region where the vertically polarized beam interacts with the sample defines the scattering volume (SV). In this study, we probe the sample using a small angle static light scattering (SASLS) technique based on the design of Ferri [70], and applied extensively to aerosols by Sorensen and his students. This design includes a Fourier lens, a beam stop, and an imaging lens. The Fourier lens is placed at one focal length's distance from the center of the scattering volume. The Fourier image of the scattered light is brought to convergence in a plane at the back focal plane of the Fourier lens. All scattered light at the same angle θ is mapped by the Fourier lens in a ring of radius r from the optical axis. Each ring of scattered light comes at the same angle θ, hence the same q, as given in Eq. (2). An imaging lens IL was used to scale the Fourier image from the Fourier lens into the 512-pixel photodiode array (PDA) (Hamamtsu, model S3902-512) detector. Most of the light that comes directly from the laser, even passes through the scattering volume, will go un-scattered, in the direction of θ = 0. To eliminate the un-scattered light (in the forward direction) a beam stop is placed at the focal length of L_1. The beam stop is a metal cylinder with a 45° surface and acts as a mirror reflecting the un-scattered light to a beam dump away from the detector. Finally, the detector will detect any visible light. Flames radiate like a blackbody; hence, they emit light. Therefore, a bandpass filter (Thorlabs) was used to allow only the 532nm wavelength to pass through and suppress all other wavelengths that resulted from flame emission.

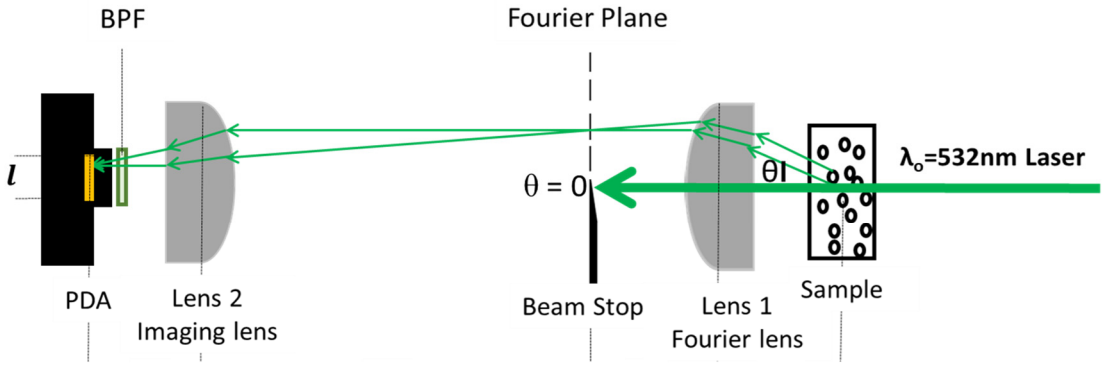

Figure 4. Schematic diagram of SASLS

The optical components for the setup, generally discussed above, were altered according to the different experiments that took place. For example, if the scattering volume were to be contained in a 3.8 cm diameter glass tube, then the Fourier lens was different from when the scattering volume was inside the 38 cm chamber. The different experimental configurations are discussed below followed by the optical adjustments and modifications unique to each of these experiments.

2.2. Experimental Variations

2.2.1. Burning and Scattering Volume Outside the Chamber

Two identical dental alcohol wick lamps (Amazon) were purchased. Kerosene and toluene (Aldrich Chemical Company) were used without further purifications as two liquid fuels with different TSI. In this configuration, the chamber was not used. Instead, a table-top wick lamp was placed such that the laser beam was between 130 mm above the 5 mm wick. Placing a small funnel at top of the flame created a steady quasi-laminar flow in the smoke, as shown in Figure 5. This was repeated for toluene. Here the laser beam passed through the smoke as shown in Figure 5(b) and this determined the scattering volume (SV).

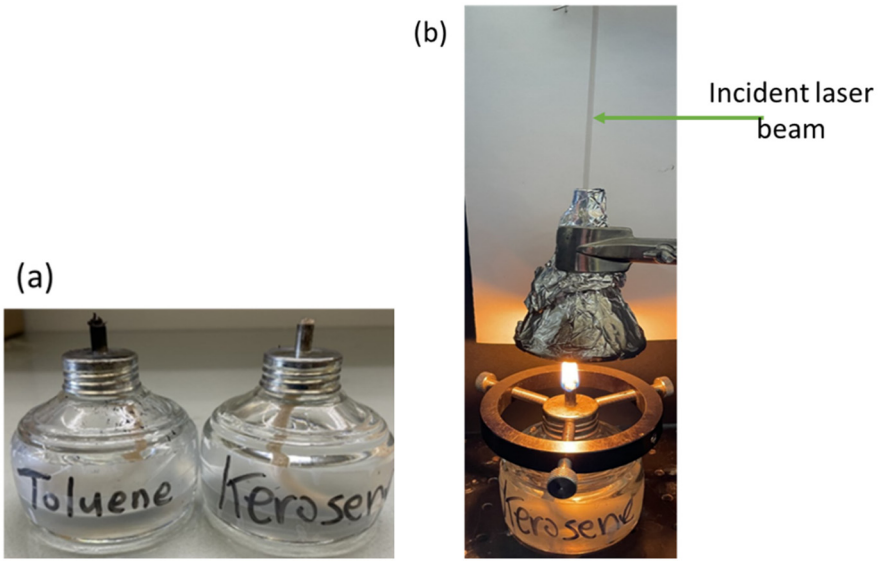

Figure 5. a) dental wick lamps and (b) soot quasi-laminar flow as it exited the funnel.

2.2.2. Burning Inside the Chamber but Scattering Volume Outside the Chamber

A 75 mm diameter glass petri dish with 20 mm height sat at the bottom of the chamber. The liquid fuel was heated through a hot plate under the solid stainless-steel bottom of the chamber. Heating was required for the kerosene liquid as it did not ignite at room temperature [2]. A small port in the chamber was used to insert a butane lighter (Olympia GM-3X) through the chamber wall to ignite the fuel. The ambient air was drawn into the system through an inlet filter (Solberg FT-19P-150) and 50.8 mm steel tubing. The steel tubing was connected through adaptors to a 38 mm diameter glass chromatography tube. The glass tube was positioned in the SASLS setup such that the laser beam passed through the center of the glass. The chamber was fastened to a heavy-duty XY-translational stage. The chamber, steel tubing, and glass tube were a rigidly connected system. This configuration allowed for fine control of the glass tube position in the setup. An 80-20 extruded aluminum structure was designed to hold the glass tube vertically with respect to the incident laser beam. The region where

the laser beam passed through the glass tube determined the scattering volume. The scattering volume was about 3 meters away from the flame inside the chamber. This is shown in Figure 6. The chamber is connected to a variable speed blower, which creates the necessary suction to pull the soot from the flame into the scattering volume. The chamber design allowed the air to flow around the fire and carry the soot up to pass through the steel tubing. After the scattering volume, the soot was passed through three aerosol capture filters. The first filter is a stainless steel filter (Kurt J. Lesker 848S2) which collected any hot particles, followed by a HEPA filter (PFIHE848), then carbon filter (PFIACG848) to capture vapor. A detailed description of the chamber design, air, and fire dynamics can be found in Ref. [3].

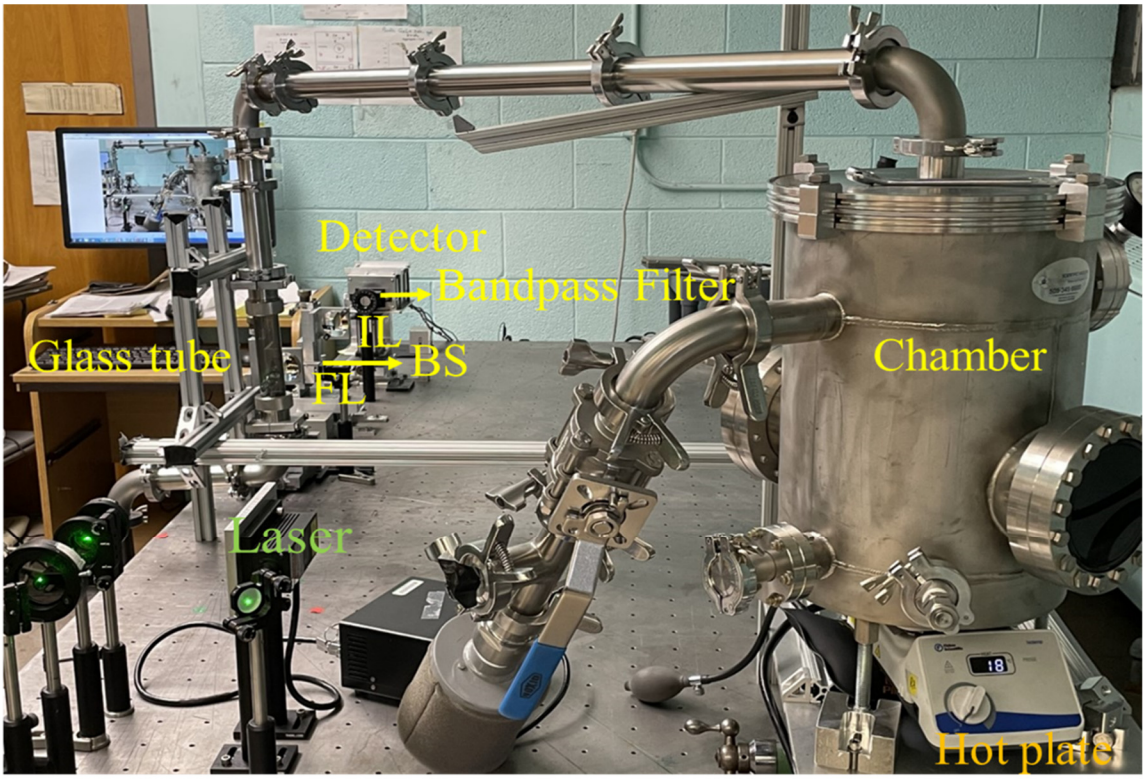

Figure 6. Experimental system consists of chamber, steel tubes, and glass tube integrated into the optical setup.

2.2.3. Burning and Scattering Volume Inside the Chamber

A 55 mm diameter glass petri dish with 20 mm height sat at the bottom of the chamber. Again, the liquid fuel was heated through a hot plate under the chamber. The glass tube was removed, and aerosols were captured by the course, HEPA, and carbon filters as in the original setup described by Hubbard et al. In this setup, the entire chamber was placed in the path of the incident laser beam. The laser beam entered the chamber through a flange mounted glass window as shown in Figure 7. There was a similar glass window at the opposite side where the scattered light exited the chamber. In this experimental configuration, the beam passed through the hot flame. The combustion and scattering volume were both inside the chamber.

Figure 7. Experimental setup incorporating the chamber directly in line with the optical setup.

The major optical component that needed to change amongst the experimental configurations was the Fourier lens. That is because the scattering volume needed to be one focal length away. For the first and second experimental variations, no adjustment was needed. The Fourier lens (AC508-80-A, Thorlabs) and IL (AC508-100-A, Thorlabs) have a diameter of 50.8 mm and focal lengths of 80 mm and 100 mm respectively. The detectable range of the scattering angle in this case was ~ 0.1° – 14°. Whereas for the third variation (where the laser passed through the chamber), the Fourier lens needed to have long focal length because the Fourier lens was outside the chamber. The Fourier lens in this case was a plano-convex lens with focal length equal to 200 mm and a diameter of 100 mm (Edmund Optics, N-BK7). The detectable range of scattering angle was approximately 0.1°-11°. All the lenses used in this study had an anti-reflection coating.

2.3. Setup Calibration

A single slit (ss) 10 μm wide and 3 mm long (Thorlabs, S10K) was used for optical calibration in all three experimental variations. A single slit calibration was performed in open air, inside the glass chromatography tube, and inside the chamber for the first, second, and third variation respectively as shown in Figure 8. The red solid line shows single slit diffraction theory and circles indicate the calibration data. The power law regime fits to a slope of -2, where d in this case is one for the single slit. Figure 8(a) shows the calibration in open air for the first experimental variation indicated by blue open circles. Additionally, it shows the calibration inside the glass chromatography tube for the second experimental variation. These two calibrations aligned well with each other as well as with the theory

all the way to the fourth peak (q = 30000 cm^{-1}). Figure 8(b) shows the calibration inside the chamber. The calibration fit the first and second peak well but was skewed to the left for the third peak (q≃19,000). for this reason, data taken inside the combustion chamber were disregarded after q≃19,000). Therefore, the smallest size detectable inside the chamber was larger than outside the chamber since q^{-1} represents the experimental length scale; the measurement range was reduced inside the chamber due to the presence of the windows, flanges, and altered optics. However, the chamber is an important engineering control when studying hazardous materials. Thus, we examined both configurations to determine the limits of light scattering measurements inside the chamber.

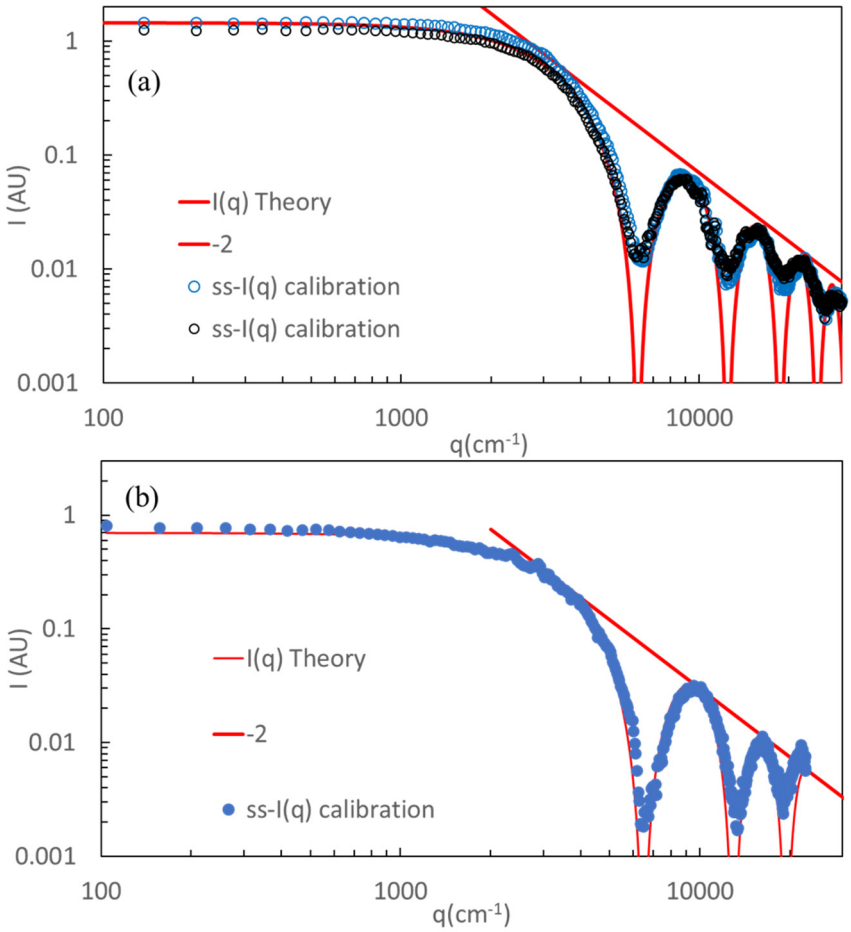

Figure 8. Single slit calibration. Circles are the experimental data, and the red lines are fit to the theory. The envelope fits a slope of -2. (a) calibration in open air and inside the glass chromatography tube, represented in blue and black circles respectively. (b) calibration inside the chamber.

2.4. Preparing the Surrogate Waste

A detailed procedure is provided in Hubbard et al. [2]. The chemicals include TBP, kerosene, and $Yb(NO_3)_3.6H_2O$. All materials were purchased from Aldrich Chemical Company and used without additional purification. A stock solution of 30% TBP-kerosene was prepared under ambient conditions by pouring 30 mL of TBP into 70 mL of kerosene. The mixture was stirred for 30-60 minutes until the two liquid phases were no longer distinguishable to the eye. This stock solution was then stored in a sealed glass bottle where the stir bar was removed. For surrogate preparation, 10

grams of $Yb(NO_3)_3.6H_2O$ was added to 100 mL of well-mixed 30% TBP-kerosene mixture. Stirring for 24 hours in addition to slightly warming the solution for about an hour was needed for the solution to be free from any precipitates. It was observed after about 6 -7 months of storage, the TBP and kerosene liquids separated, with or without the metal nitrate. In this case, stirring procedures were repeated and no solid precipitates were observed before starting any experiment. The sample which had separated and was remixed will be referred to as "old sample" in the discussion section. New stock was also prepared, which were one day old from the time doing the experiments. Using this stock will be referred to as "new sample" in the discussion section.

3. RESULTS AND DISCUSSIONS

3.1. Burning and Scattering Volume Outside the Chamber

In this experiment, two identical wick lamps were used, one for each of the liquid fuels kerosene and toluene. The scattering volume was 130 mm above the wick burner. The chamber was not used. The experimental scattered intensity, I(q), plotted vs. q, on a double logarithmic scale is shown in Figure 9.

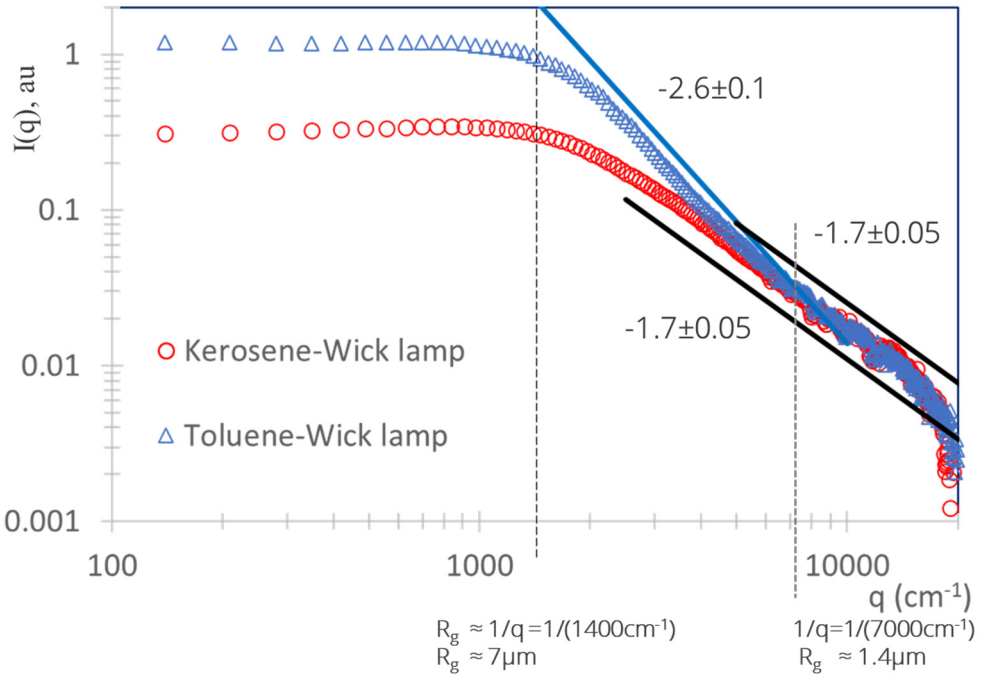

Figure 9. I(q) vs. q on a double logarithmic scale for kerosene (red circles) and toluene (blue triangles) at 130mm height above the wick burner.

The kerosene data in Figure 9 (red circles) show the kerosene soot formation followed the standard DLCA morphology characterized by $D_f = 1.7 \pm 0.05$. Additionally, the Guinier regime indicated that the average size of the aggregates was about $1/q \simeq 1/(1400\text{cm}^{-1}) \simeq 7\mu\text{m}$. Whereas for toluene, the data shows two morphologies. The first one occurred at larger q values, hence at shorter length scales (~1.4 μm) with a $D_f = 1.7 \pm 0.05$. The second morphology occurred at smaller q values, hence larger length scales (~ 7μm) with a $D_f = 2.6 \pm 0.1$. The transition between 1.7 to 2.6 morphologies occurred at about $1/q \simeq 1/(7000\text{cm}^{-1}) \simeq 1.4\mu\text{m}$. These results are consistent with the super-aggregates first documented by Kim et al. [14], [15]. Toluene is much sootier than kerosene with a TSI >10 [14], [15]. This explains why the super-aggregate structure was observed only for toluene. Additionally, these super-aggregates had a length scale of approximately 7 μm and were made of the smaller 1.7 DLCA aggregates, which were observed at about 1μm length scale.

Key takeaways

- Burning toluene and kerosene fuels produced fractal soot aggregates formed via the DLCA mechanism with D_f=1.7.

- A super-aggregate structure, which is a hybrid structure, was observed for the sootier toluene fuel as expected.

3.2. Burning Inside the Chamber but Scattering Volume Outside the Chamber

For the second experimental variation, the open pool fire took place inside the chamber and the scattering volume was outside the chamber. In this case, the soot travelled about 3 meters to reach the scattering volume inside the glass chromatography tube. Soot transport was driven by the blower. Figure 10(a) shows the scattered intensities for kerosene. It appeared that the aggregates had a fractal morphology with $D_f = 1.6 \pm 0.1$ and the average R_g at the Guinier regime was about 7.5μm. This Guinier regime is rather broad qualitatively indicating a broad distribution of sizes. The average size of soot produced inside the chamber was sub-micrometer in size ($\simeq$ 0.5μm), much less than the 7.5 μm size measured in Figure 10. That is because the 3 meter distance to reach the scattering volume provided sufficient time for soot particles to further grow and form bigger aggregates.

Additionally, Figure 10(a) shows a distinct Guinier regime feature when compared to the Guinier regimes in Figure 9. Recall that the Guinier regime is the regime connecting the Rayleigh regime to the power law regime in the scattered intensity double log plot, I(q) vs. q (section 1.1.2., Figure 3). To make the comparison easier, Figure 9 and Figure 10(a) are plotted together and shown in Figure 10(b). The Guinier regimes are highlighted in light grey color. The Guinier regime is defined here when the Rayleigh regime scattered intensity, I(0) falls to about two-thirds off its initial value. The end of this regime is roughly taken when the power law slopes no longer fit the data. The shaded Guinier regime for the solid red circles, which are the data collected in this section, clearly extends further than the other two plots.

Gautam et al. [48] combined many ADLS techniques to study hematite aggregates. The scattered intensity collected from their small angle light scattering setup provided the Rayleigh and Guinier regimes in the scattered intensity plot. They found a Guinier regime with a slope of -0.5 and they referred to it as an extended Guinier regime. They captured optical microscope images for the hematite aggregates, which showed a bimodal distribution with mode sizes roughly about 1 μm and 10 μm. The smaller aggregates were the dominant number in this distribution. Additionally, they calculated the diffraction pattern representing the hematite aggregates and their bimodal distribution. When added together, these diffraction patterns showed a slope of -0.5 as seen in their experimental data. They concluded that the bimodal distribution caused the extended Guinier regime.

Figure 10(b) shows an extended (broad) Guinier regime for the data collected at 3 meters from the flame with a slope of -0.8 ± 0.2. In summary, the extended Guinier regime may indicate significant polydispersity. Future work will aim to collect soot samples at this scattering volume and perform SEM and optical images to draw a conclusion about this extended Guinier regime. This is important to know whether the chamber, blower speed, and even the distance the soot travels before reaching the scattering volume has any influence on the aggregate size distribution.

The same experiment was repeated for toluene, but no signal was collected due to the high toluene soot deposition on the glass chromatography tube, see Figure 10(c). Toluene soot deposition obscured the light signal. Kerosene soot deposition on the glass chromatography tube was also observed, however, the amount of deposition was much less than toluene and the kerosene signal was detected. Therefore, caution is needed when analyzing the I(q) vs. q graph for kerosene. For example, in Figure 10(a) the slope of 1.6 is smaller than the common 1.7-1.8 reported fractal dimension for DLCA

aggregates[5], [6], [17], [40]. This might be due to slight soot deposition on the glass tube. Consequently, a nitrogen purged glass tube design is being implemented in year 3 of the project to eliminate soot deposition.

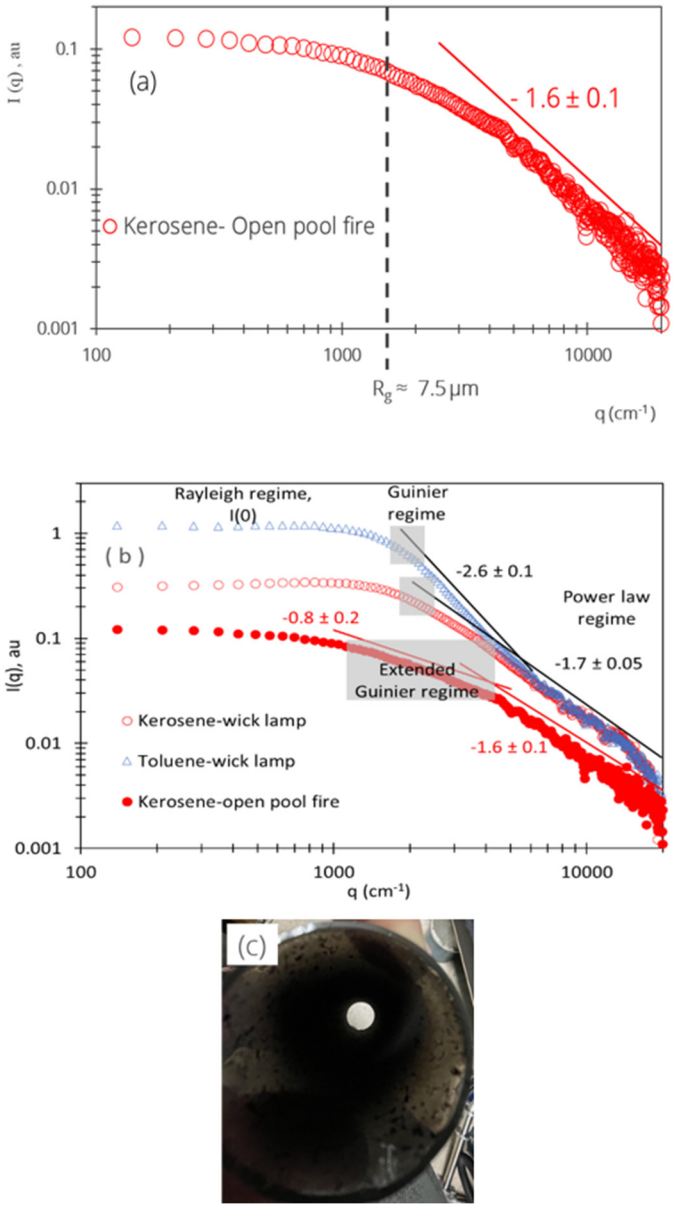

Figure 10. (a) I(q) vs. q for the pen pool fire placed inside the chamber and scattering volume outside the chamber (about 3 meters far from the flame). (b) comparison between the Guinier regimes for the data obtained in (a) and in Figure 9. (c) Toluene soot deposition on the glass tube.

Key takeaways

- At meter scale distances from the flame, aggregates had the chance to grow and form large aggregates.
- The "extended Guinier regime" could be attributable to aerosol polydispersity or obscuration from soot deposited onto walls of the glass tube.

3.3. Burning and Scattering Volume Inside the Chamber

For the third experimental variation two burning mechanisms took place inside the chamber: a 10 mL wick lamp and an open pool fire. In both cases the scattering volume was defined by the laser beam passing through the luminous flame itself inside the chamber. Different liquid fuels were used for each of these burning mechanisms.

- 10 mL wick lamp
  - kerosene and toluene
- open pool fire
  - kerosene (K), K/TBP, K/TBP/Yb.

3.3.1. 10 mL wick Lamp

The 10 mL wick lamp was made of 10 mL glass beaker with a glass cap cover set on top of the beaker. A hole was made in the glass cap for the wick to pass through. This is shown in Figure 11(a). Kerosene and toluene were the two liquid fuels used in the 10 mL wick lamp. The same wick glass structure was used for both fuels after thorough cleaning and drying, but the wick itself was changed for each fuel.

Figure 11(b) shows the scattering intensity on a double logarithmic scale for toluene and kerosene flames. The toluene flame produced soot aggregates with a fractal dimension of 2.5 and a Guinier size, radius of gyration of Rg $\simeq$ 7.5 μm. Kerosene burning produced particles submicron in size ($\simeq$ 0.6 μm). For kerosene the change in slope occurred around the data cut off where data were disregarded ($q \simeq 19{,}000 cm^{-1}$) such that the slope, hence the morphology of the aggregates, was undetected. However, although we could not quantify the soot size or morphology, we can qualify that all particles were respirable. This is important and is often an assumption made in safety assessments (RF=1).

This figure shows a clear distinction in light scattering plots for flames produced from burning fuel with different TSI. The distinction is clear in soot size, and possibly soot morphology. After burning toluene, the chamber lid collected more char than kerosene (of the order of millimeters in thickness). The chamber windows required extensive cleaning due to high toluene soot deposition.

Both results in Figure 11(b) and Figure 9 were produced from burning kerosene and toluene from wick lamps, however, the results were noticeably different. These differences can be attributed to two major changes. First, the scattering volume in Figure 11(b) passed through the luminescent flame itself and not the smoke as in Figure 9. Additionally, the air dynamics surrounding the flame inside the chamber are quite different than the air dynamics for the simple wick burning outside the chamber. Hence, we should not necessarily expect similar results. For example, Figure 11(b) (inside the chamber) shows only the 2.5 morphology of toluene and no evidence of the 1.8 morphology. This might indicate denser aggregates for burning inside the chamber. We hypothesize shear forces inside the chamber could result in denser morphology [8]. Denser morphology was also formed by shear-induced fragmentation in colloidal aggregates [9], [10], [51], [52], [53].

Aggregate compaction can result in increasing the fractal dimension from the common 1.8 for DLCA aggregates to higher values of approximately 2.5 [9], [10], [11]. The coating mechanism discussed earlier can also result in more compact aggregates. The condensation of water vapor or combustion products may lead to dense structures with fractal dimension up to 2.5 [12], [13]. In the current set of experiments, ambient air was pulled into the chamber. The experiment was done in Manhattan, KS during June with average outside summer humidity ranges from 67% to 76% [71]. Furthermore, combustion vapor might be a byproduct of burning liquid fuel from a wick lamp which subsequently

condenses onto the surface of soot particles. Previous results from burning toluene in the wick lamp outside the chamber, as shown in Figure 9, showed both 1.8 and 2.5 morphologies. This indicates, but not confirms, that the restructuring observed here is probably not related to the coating mechanism but rather to the influence of shear. The appearance of one compact structure for burning toluene from a 10 mL wick lamp, resulting in $D_f = 2.5$, should be examined in future studies.

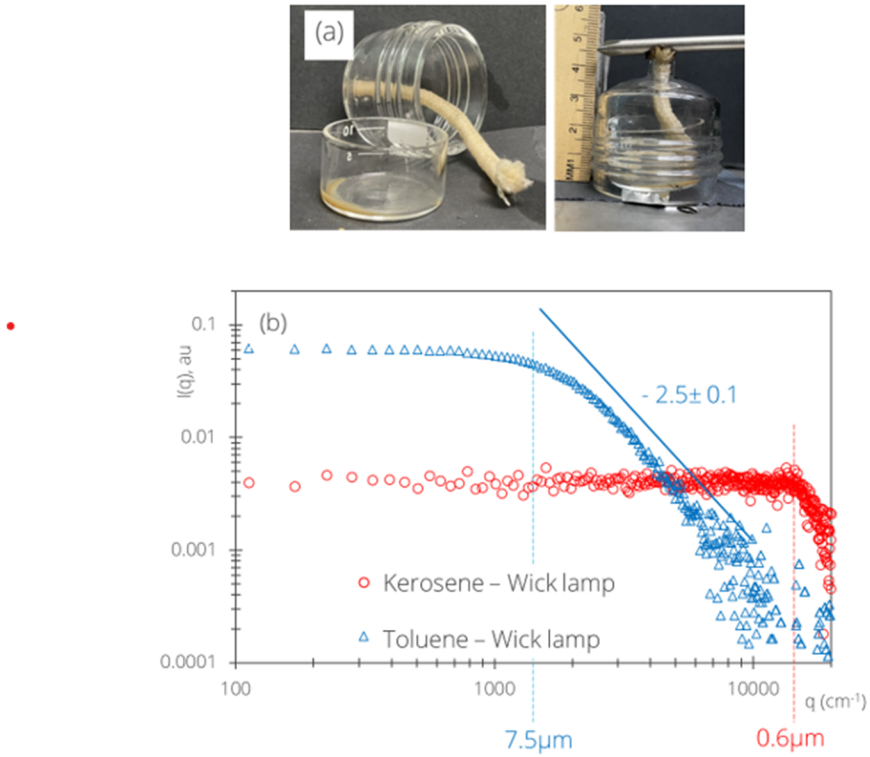

Figure 11. (a) Image of the 10 mL wick lamp. (b) I(q) vs. q on a double logarithmic scale for kerosene (red open circles) and toluene (blue open triangles).

The chamber design in this experiment provided blower speed control. Due to the severe toluene soot deposition on the glass windows, kerosene was the only fuel used hereafter. Kerosene is also a constituent of nuclear waste streams and has been used in the previous works of Hubbard et al. [2]. Figure 12 shows the scattered intensity for kerosene burning from a 10 mL wick lamp where blower speed settings were 0, 25, 35, 45, 55, 65, and 72. These speed settings were not currently calibrated to air flow rate, hence have no units. In future experiments, a velocity probe will be used to calculate the volumetric flow rate through the chamber. This figure shows the collected scattered intensity data at each blower speed. Each plot contains the total number of data collected. The blower setting jumped from 0 to 20, so 20 is the lowest value where air flowed into the chamber. The exposure time in collecting each dataset was 20 msec, which is the fastest collection time the detection system can achieve. The use of the 20 msec exposure time is to provide data on the statistics of fluctuations. Therefore, each intensity curve represents a snapshot in time. These snapshot intensities will be referred to as time varying scattered intensities. The flames were stable and behaved like laminar diffusion flames due to the presence of the chamber airflow. Flame stability was assessed both by eye and based on the stability of the light scattering signal at the beginning of each experiment.

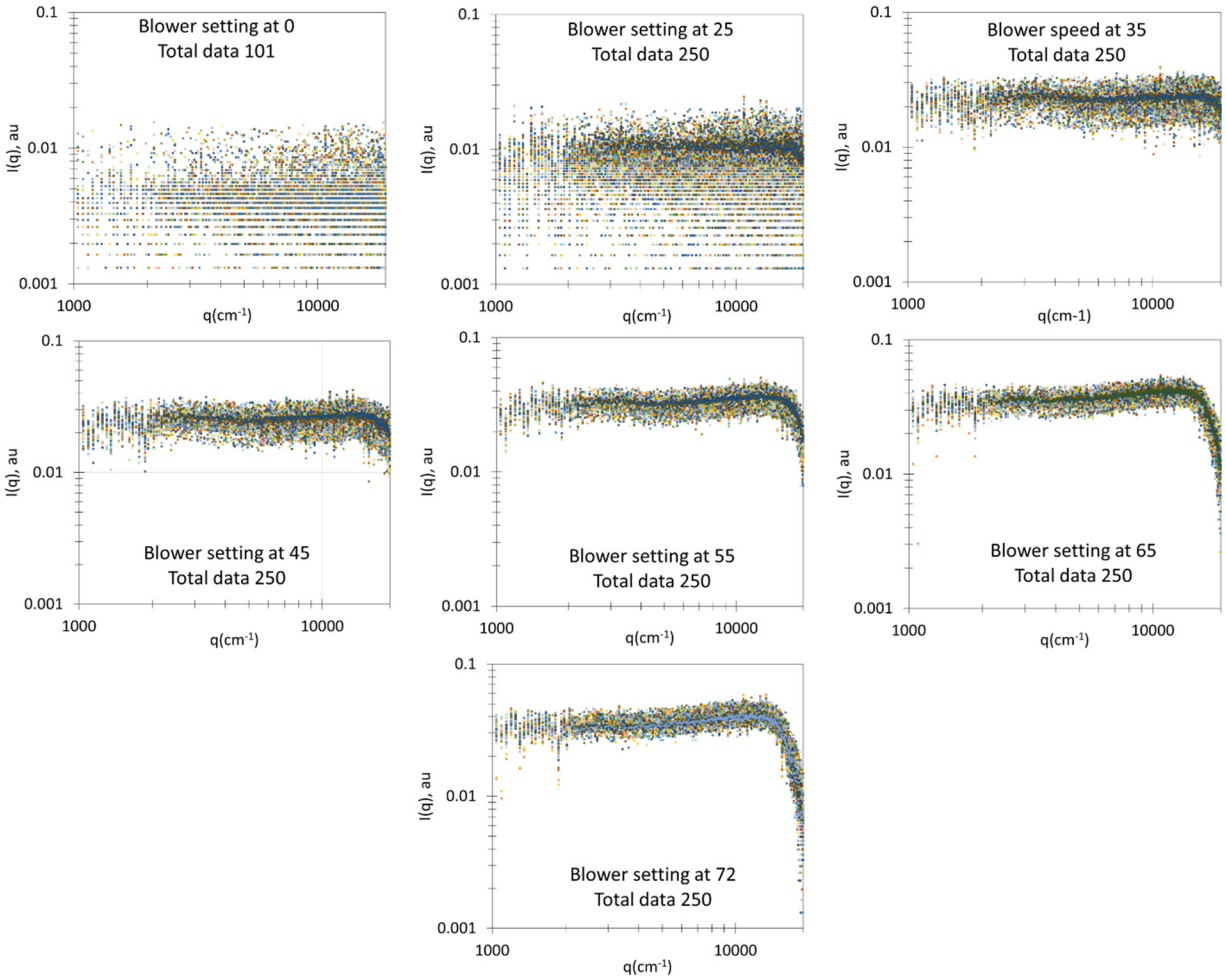

Figure 12. 12 I(q) vs. q in a double logarithmic scale for buring kerosene in a 10 mL wick lamp for different blower settings.

In Figure 12, the collected intensities for a blower speed of 0 were comparable to the background measurements before igniting the wick. At blower speed of 25, the signal started to distinguish itself from the background, but the intensity was constant throughout the q range, hence showing only the Rayleigh regime, I(0). In both cases, the aggregate size at these speeds were smaller than the detectable limit of about 0.6 micron. In contrast, settings with blower speeds greater than 35 show that a Guinier regime starts to develop. This indicated that the aggregates were growing. Additionally, I(0) increases with increasing blower speed. For this reason, the time varying intensities were averaged for each speed and plotted vs q.

Figure 13(a) represents average intensity data. It is clear from this Figure that the average Rayleigh intensity, I(0), increases with higher blower speed and that the Guinier regime moves to smaller q values, indicating larger aggregate sizes. From Figure 13(a), the average of I(0) and R_g was obtained, where possible. These R_g values represent a type of average as they are obtained from time-averaged curves. It was found that the smallest average R_g was detectable at blower speeds ≥ 45.

The average I(0) vs. R_g for each speed is plotted in Figure 13(b). This figure shows scattering intensity in the Rayleigh regime I(0) and aggregate size are related to the blower speed. This shows that blower speeds inside the chamber has an affect on the light scattering signal. Blower speed can affect flame dynamics and soot production as well as soot aggregation.

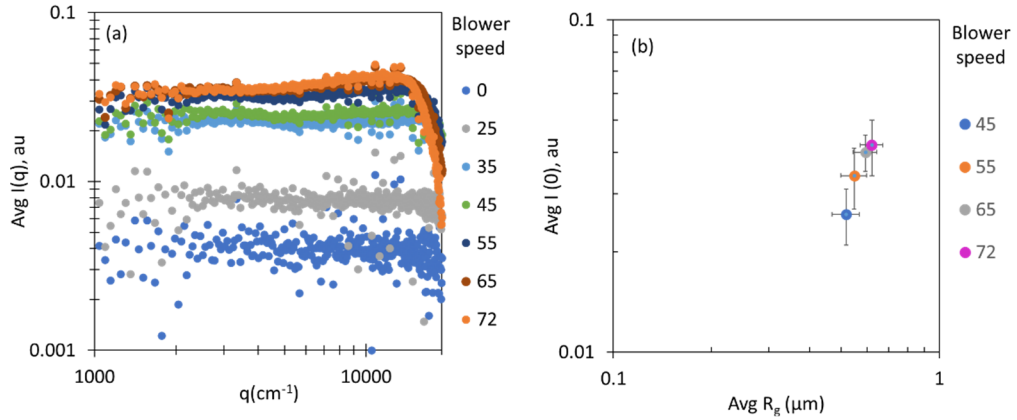

Figure 13. Double logarithmic scale for (a) Avg I(0) vs. q for burning kerosene in 10ml-wick lamp as a function of different blower speeds. (b) Avg I(0) vs. Avg R_g obtained from the data in Figure 12(a).

Key takeaways

- Aggregates formed inside the chamber from the toluene flame were distinctly different from those produced from a kerosene flame using the 10 mL wick lamp.
- Blower speeds inside the chamber affect the light scattering signal through flame and aerosol dynamics.

3.3.2. Open Pool Fire

For the open pool fire configuration, a 55 cm diameter petri glass dish was used for the final experimental variation where the scattering volume and burning were both inside the chamber. The scattering volume was defined by the region where the laser passed through the flame. Here, three different fuels were used: kerosene (K), K/TBP, and K/TBP/Yb. Different blower speeds and detector exposure times were also used. Experiments were conducted and data were collected according to the information in Table 1.

Table 1. Summarizes the different experiments done for OPF inside the chamber.

Fuel type (old vs. new)	Blower speed settings	Exposure time	Total # of data	Number of tests	Flame stability
K	30, 50, and 70	20msec	250	1	Stable
K/TBP (Old sample)	30, 50, and 70	20msec	500	2 (Test1 and Test2)	Stable For both tests
K/TBP/Yb (Old sample)	30, 50, and 70	20msec	500	2 (Test1 and Test2)	Not stable For both tests
K/TBP/Yb (New sample)	30, 50, and 70	20msec	500	1	Stable
K	30 and 50	200msec	250	1	Stable
K/TBP (New sample)	30 and 50	200msec	500	1	Stable
K/TBP/Yb (New Sample)	30 and 50	200msec	500	1	Stable

Figure 14 represents an example of the data summarized in Table 1. Time varying intensities were plotted for each fuel type: K, K/TBP (old sample, Test1), and K/TBP/Yb (old sample, Test1) with the corresponding blower speeds: 30, 50, and 70. Flames were stable for most of the data. However, in the experiment with K/TPB/Yb at blower speed of 70 the fuel level was low, therefore, the signal fluctuated, leading to an unstable flame.

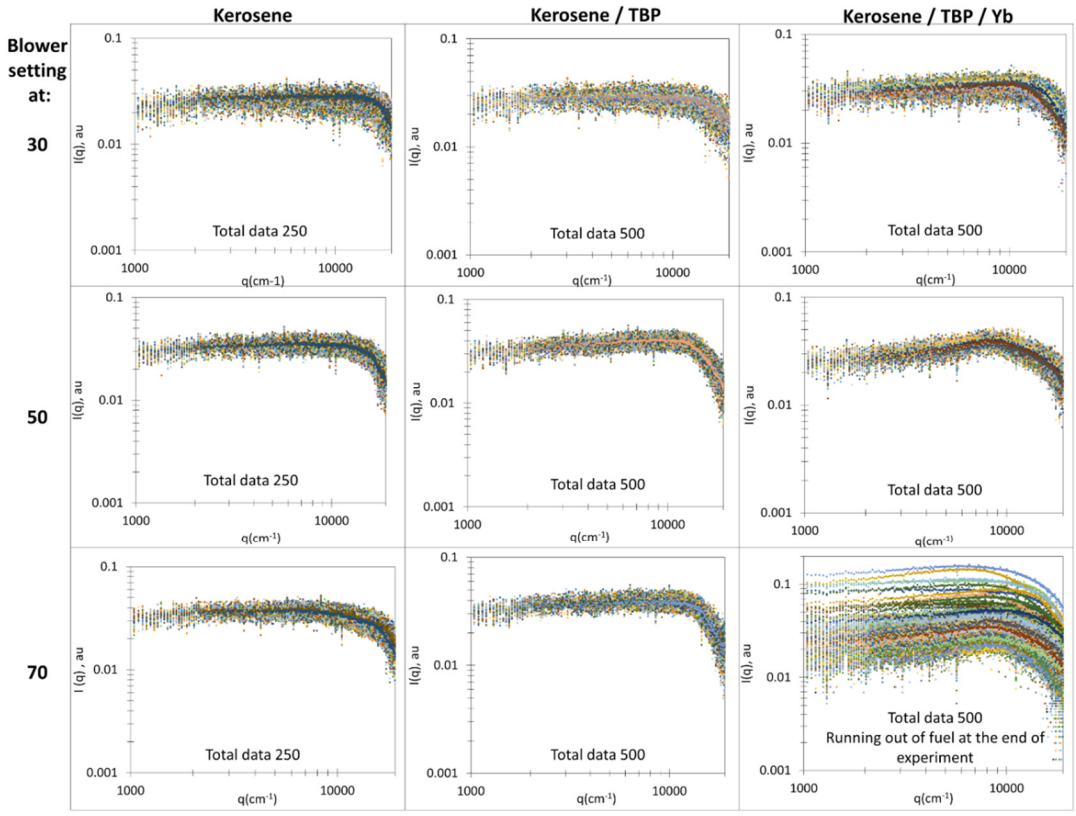

Figure 14 I(q) vs. q in a double logarithmic scale for open pool fire burning kerosene, Kerosene/TBP, and Kerosene/TBP/Yb for blower speed settings at 30, 50, and 70.

3.3.2.1. Analysis of Average Scattered Intensities

To investigate whether the blower speed changed the production/growth of aerosol, the average scattering data was obtained for the different stable flames summarized in Table 1. The average intensities for each fuel type were plotted as a function of blower speed as shown in Figure 15. In general, blower speed seemed to influence the average intensity signal. The higher the blower speed the higher the Rayleigh scattering intensity, I(0). Increased blower speeds also pushed the Guinier regime into smaller q values (larger particles). This is consistent with the previous finding with the average intensity data when using the 10 mL wick lamp. However, one set of data did not show this general trend. This set of data is represented in Figure 15(d) which is K/TBP/Yb "old sample". This set was repeated twice and in both cases the sample ran out of fuel quicker than the rest. Meanwhile, when a new sample was prepared, fuel depletion was not an issue. It is plausible that the age of the sample influences the aerosol production. This variable will be removed in future experiments.

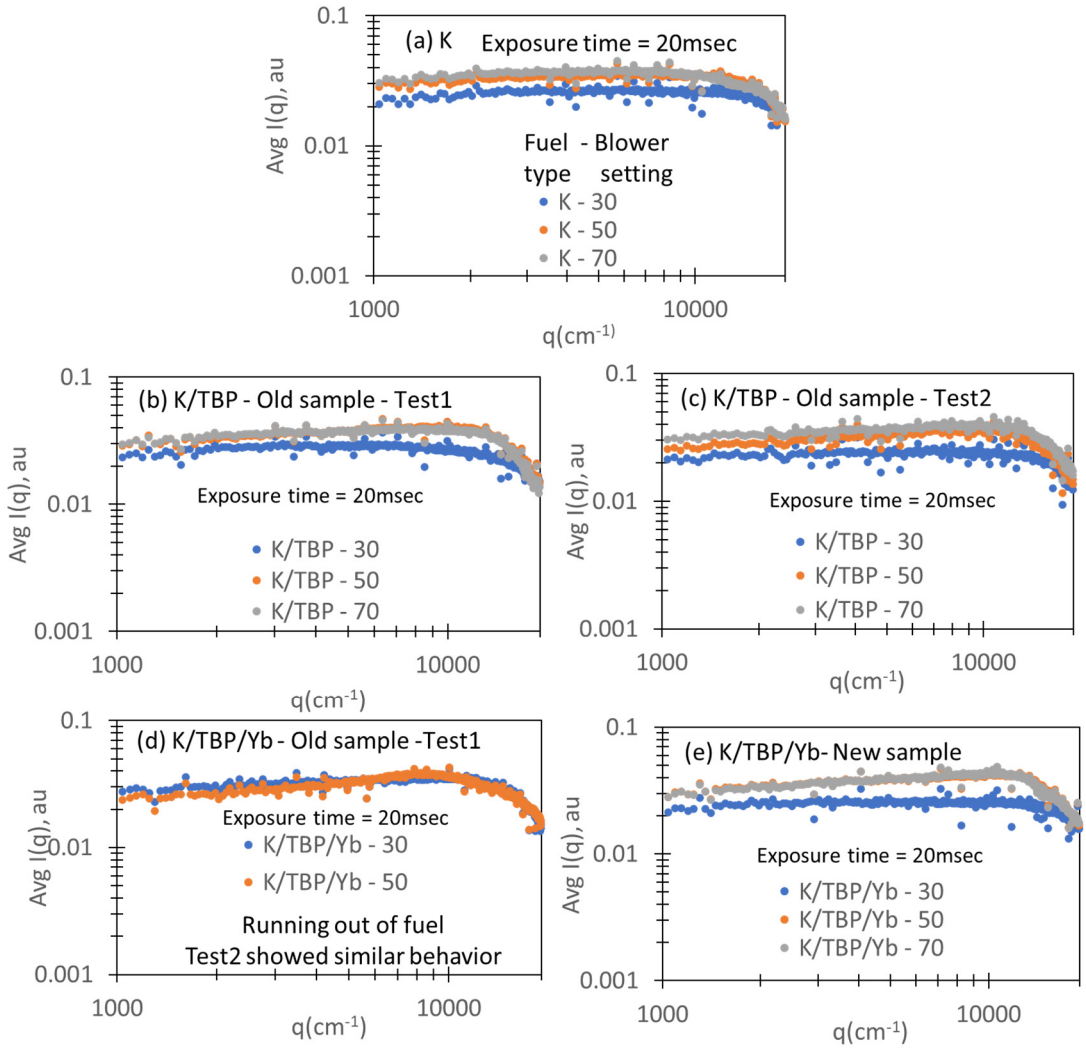

Figure 15. Average scattered intensities for different fuel types plotted as a function of blower speeds.

The average Rayleigh scattering, Avg I(0) and the average R_g was obtained from data in Figure 15. These averages are plotted for the different fuel types and speeds in Figure 16. Similar to what was observed in the 10 mL wick flames, higher blower speeds increased the average Rayleigh scattering intensity and aggregate size.

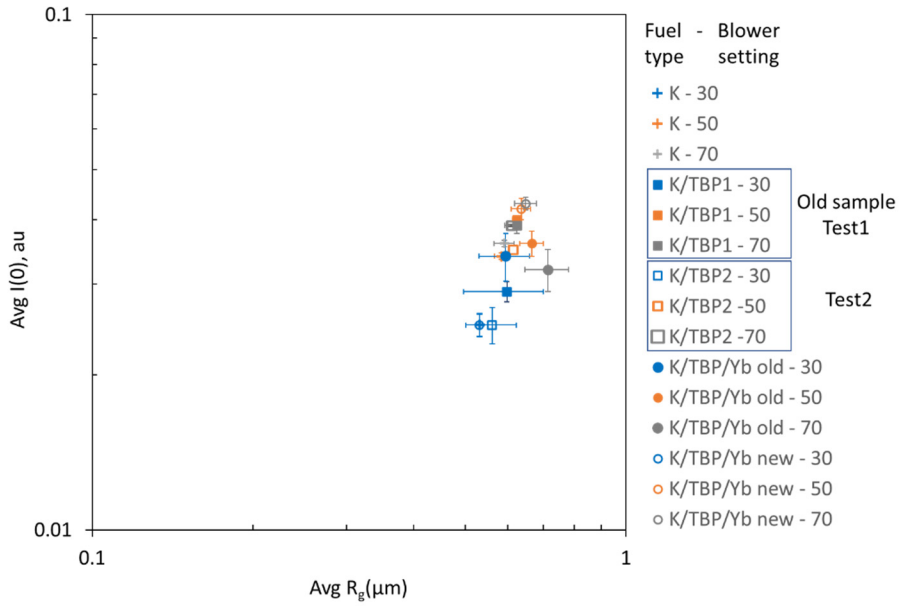

Figure 16. Avg I(0) vs R_g in double Logarithmic scale for different fuel types and blower speeds for data summarized in Table1. Blue, orange, and grey colors represent blower setting 30, 50, and 70 respectively.

To address whether fuel type influenced the scattered intensity signal, average intensities were plotted as a function of the fuel type for each blower setting. It was found that some data lay on top of each other.

Average data were multiplied by constants for visual comparison in the shape of each curve. This is shown in Figure 17. Blower speeds are presented in separate subplots: (a) 30, (b) 50, and (c) 70. Each subplot contains all the different fuel types. This figure is plotted on a linear-log scale. The figure shows for speed 30, all fuel types produce the same scattering profile where the light scattering intensity is independent of q all the way until the Guinier regime starts. The dashed lines in these figures are flat for visual comparsion to the data.

For blower speeds at 50 and 70 and fuel type K/TBP/Yb, different behavior was observed. The Rayleigh intensity exhibits some q dependence before the Guinier regime starts. The scattered intensity increases from q = 1000 cm^{-1} to the Guiner regime. The other fuel types at higher speeds do not exhibit this behavior.

There is no conclusive explanation for this behavior. However, we hypothesize that it could be due to the presence of Yb in the aerosol. Yb-nitrate is water soluable and this could enhance water condensation and aggregate restructuring. This behavior will be explored in future studies by including other metal nitrates (e.g., Lu and 238-U). If the behavior is reproduced for other metal nitrates, but never appears when metal nitrates are absent, this could be an exploitable signature for nuclear waste fire smoke containing hazardous metals.

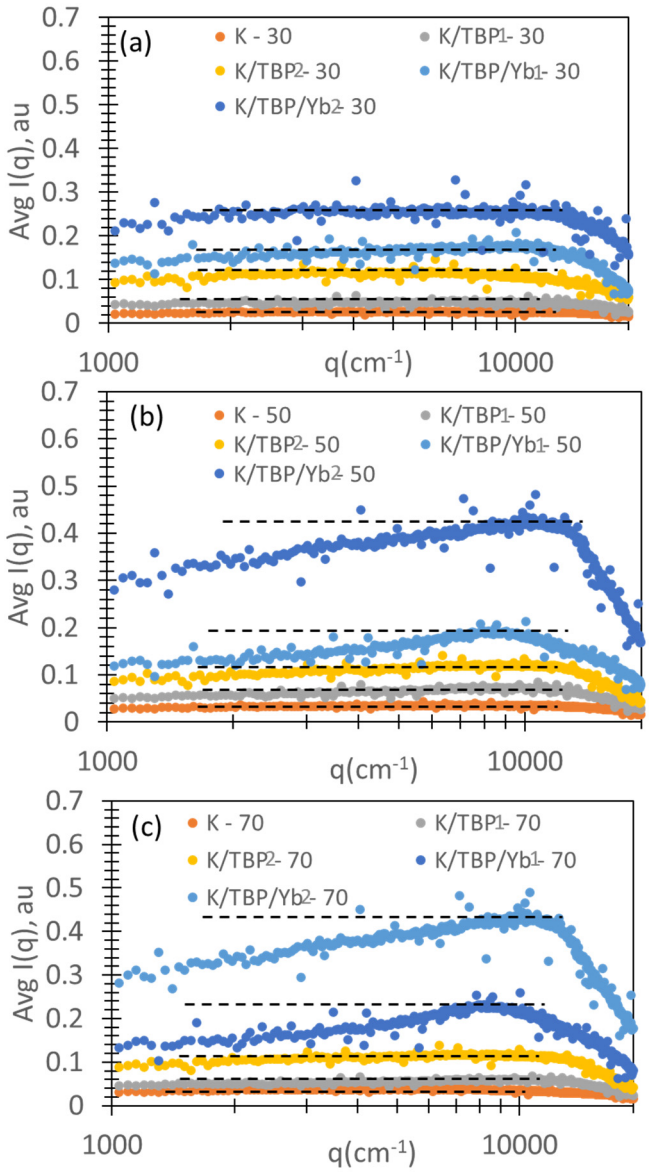

Figure 17. Linear-Log plot of Avg I(q) vs. q for different fuel types at blower setting (a) 30, (b) 50 , and (c) 70. The dashed lines are to guide the eye.

As previously mentioned, Hubbard et al. [2] studied the ARF for soot formed by burning liquid kerosene contaminated with nuclear waste surrogates Yb-nitrate and Lu-nitrate. They collected the soot and performed SEM analysis. The liquid fuel preparation and the chamber used in this work mimicked the ones used in their study. The SEM images were taken for the collected samples as presented in Figure 18 for (a) K, (b) K/TBP, and (c) K/TBP/Yb. These images show that the aggregates are compact for all fuel types. As mentioned earlier, this compaction could be caused by shear or surface condensation. In future studies, this compaction could be studied through Fourier analysis of these images. That analysis would quantify the fractal dimension of these aggregates (imaged) and compare them with the experiments (light scattering).

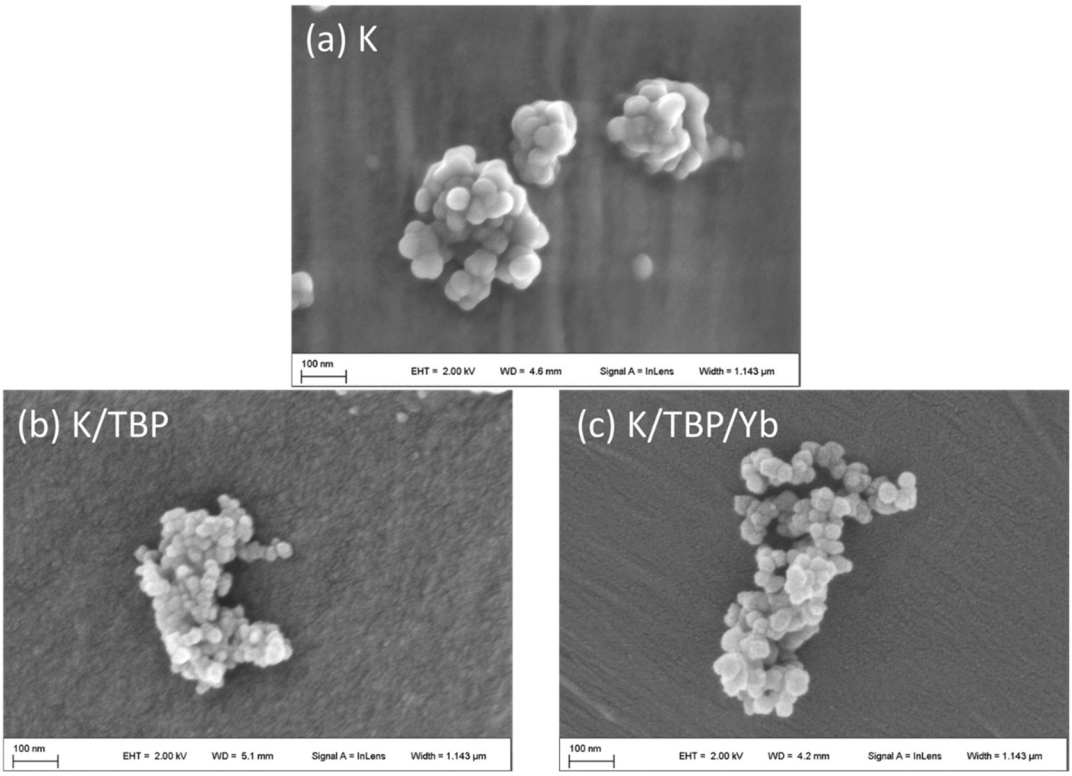

Figure 18. SEM images of open pool fire of (a) kerosene (k), (b) K/TBP, and (c) K/TBP/Yb.

Key takeaways

- Blower speed affects the scattered light signal through flame and aerosol dynamics.
- The scattered signal from K/TBP/Yb, at higher blower speeds, exhibits a q-dependence at low q, before the Guinier regime starts. This q-dependent behavior should be explored by investigating whether different metal nitrates (e.g., Lu and 238-U) exhibit similar scattering patterns.
- Future work could involve SEM image analysis to find the aggregates fractal dimension, providing corroboration data for light scattering measurements.

3.3.2.2. Analysis of time varying intensities

In addition to comparing averages, we looked at time-varying intensities I(q). Probability distribution histograms of I_o and R_g were constucted for the different stable flame experiments summarized in Table 1.

Figure 19 shows the probability distribution histograms for the Rayleigh scattered intensites, I_o. Some experiments show a separation between the scattered intensity values for blower speed at 30 compared to the other two speeds. For example, if you look at K, K/TBP (old stock) and K/TBP/Yb (new stock) for exposure time 20 msec, the magenta color histogram is more separable than the others. Magenta represents blower speed 30. This observation is consistent with the blower speed effect on the average intensity data obtained in previous sections. On the other hand, the K/TBP/Yb for the old sample shows no separation. This could be caused by fuel depletion during these experiments. Experiments performed with a detector exposure time of 200 msec also showed no separation. More work needs to be done to determine if these experiments are repeatable. Previous work by Hubbard

et al. showed ARF values that varied appreciably from experiment to experiment. It is unknown if three repeated datasets will ever show consistent behavior with respect to data shown in Figure 19.

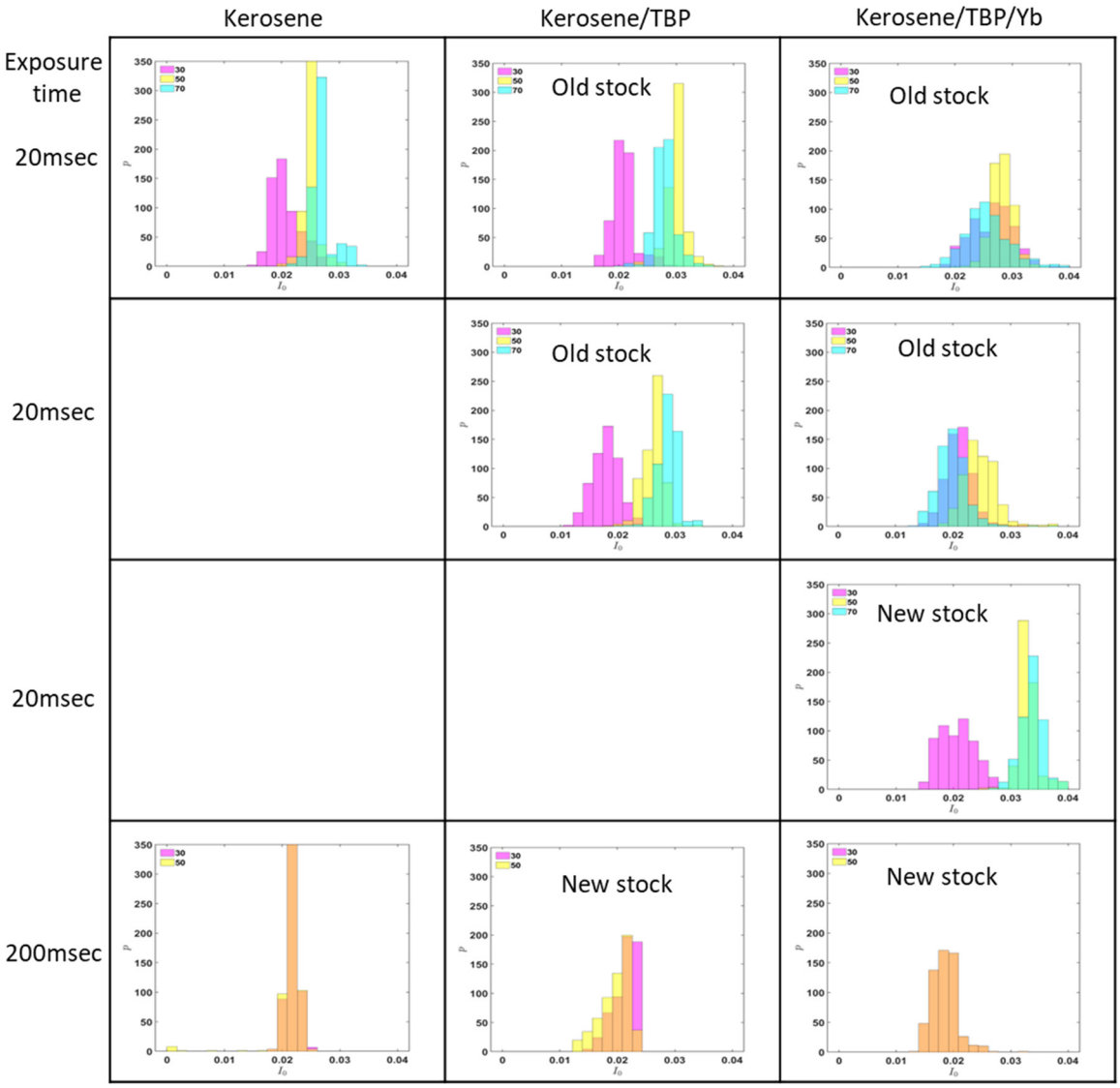

Figure 19. I_o probabililty density distributions for the different fuel types, blower speeds, scattered light acquasition time, and wether the stock is new or old. Color explanations: 30, 50, and 70 blower speeds are identified by magenta, yellow, and cyan colors. Magenta & yellow gives orange. Magenta and cyan gives purple. Yellow and cyan gives light green. Magenta, yellow, and cyane gives darker green

Guiner analysis was also preformed to obtain R_g. Figure 20 shows R_g probability density histograms for the different fuel types and speeds. Again, some data show some separtion but others did not. Additional experiments are needed to confirm this behavior is, or is not, repeatable. In both cases, I_o and R_g histograms, significant differences amongst some blower speeds can be observed in some experiments but not in others. We again refer back to Hubbard et al. [3] where the uncertainty in ARF was comparable to the mean. Figures 19 and 20 may show actual experiment-to-experiment variability, which cannot be removed through additional measurements.

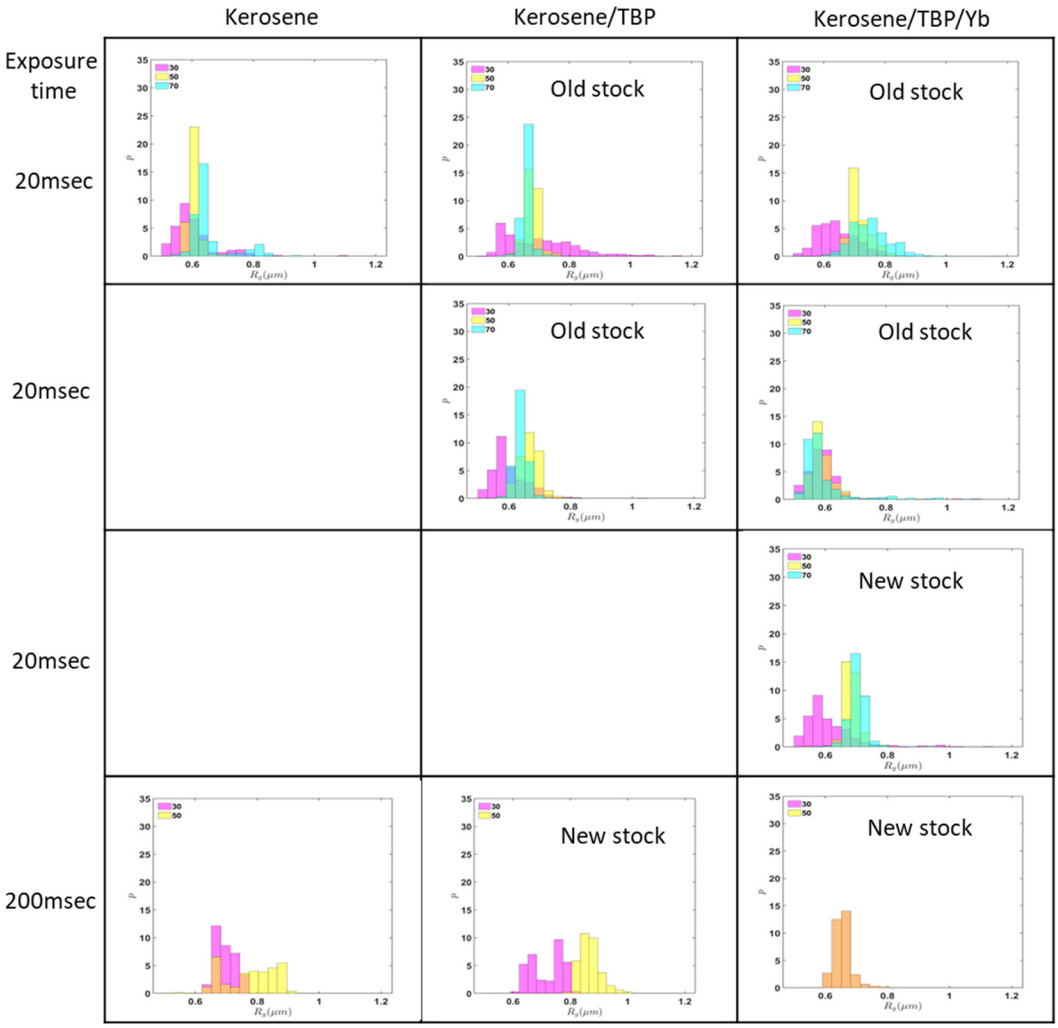

Figure 20. R_g probabililty density distributions for the different fuel types, blower speeds, scattered light acquasition time, and wether the stock is new or old. Color explanations: 30, 50, and 70 blower speeds are identified by magenta, yellow, and cyan colors. Magenta & yellow gives orange. Magenta and cyan gives purple. Yellow and cyan gives light green. Magenta, yellow, and cyane gives darker green.

Key takeaways

- Plotting histograms of I_o and R_g did not identify conclusive differences in fuel type or blower speed due to variations between experiments. Previous work by Hubbard et al. [3] showed the uncertainty in ARF was similar in magnitude to the mean ARF. For this reason, it may be reasonable to conclude experiment-to-experiment variability in aerosol production and growth is plausible.

4. CONCLUSION

In-situ characterization of soot aggregates was performed with small angle light scattering. Small fire experiments were conducted by burning liquid fuels and liquid fuels contaminated with surrogate nuclear waste metals. The goals of this work were to (1) develop and validate experimental techniques for in-situ aerosol characterization, (2) explore flame and aerosol dynamics from surrogate nuclear waste fires, and (3) determine the possibility of detecting hazardous contaminants within a carbon soot matrix.

In this study, three experimental configurations were explored. For the first variation, the laser beam passed through smoke generated from a dental alcohol wick burner. In this configuration no chamber was used to confine the flame or smoke. Kerosene and toluene fuels were used. Kerosene aggregates were about 7 μm in radius with a fractal dimension of 1.7 ± 0.05. This latter value is consistent with the DLCA morphology. Toluene, which is a sootier fuel, produced a super-aggregate hybrid morphology. These super-aggregates had a radius of about 7 μm with a fractal dimension of 2.6 ± 0.1, and were comprised of smaller aggregates 1 μm in radius with a fractal dimension of 1.7± 0.05. This is consistent with the picture first published by Kim et al. regarding super-aggregates [14].

For the second variation, a unique combustion chamber designed by Hubbard et al. [3] was employed. A kerosene pool fire was ignited inside the chamber. Even though the flame was inside the chamber, the soot particles traveled about 3 meters from the flame before entering a glass tube containing the scattering volume. The scattering intensity showed the presence 7.5 μm aggregates with a fractal dimension of 1.6 ± 0.1. In this experiment, the soot had more residence time to aggregate and grow [5]. Soot deposition onto the glass observation tube was observed. Shear effects may have been present and warrant further investigation.

For the third experimental configuration, a small 10 mL wick lamp flame and an open pool fire were investigated. The scattering volume was defined as the region where the laser beam passed through the luminous flame itself inside the chamber. The fuels used for these experiments were: (1) kerosene and toluene for the 10 mL wick lamp, and (2) Kerosene (K), K/TBP, K/TBP/Yb, for the open pool fire.

For the 10 mL wick lamp, aggregates formed from toluene combustion were distinctly different than those produced from kerosene. For kerosene, the aggregate radius was approximately 0.6 μm, near the detection limit of the apparatus. In contrast, toluene aggregates in the flame were measured to be almost an order of magnitude larger with a fractal dimension of 2.5 ± 0.1. The higher D_f value appeared for toluene flames with no super-aggregate structure implying that these aggregates might be denser than the first two experimental configuration. More compact structures might be due to either fluid shear forces [8], [9], [10], [11], condensational surface coatings [12], [13] or a combination. The mechanism of compaction is undetermined. Higher blower speeds produced larger aggregates and higher scattered intensities. It is probable that blower speed impacted both flame and aerosol dynamics. Some experiments indicated that the presence of metal-nitrate may produce distinguishable features in the light scattering signal. More work is needed to confirm the presence of this feature for other metal-nitrates.

This work demonstrated that light scattering techniques can be used successfully, in conjunction with the combustion chamber of Hubbard et al. [2], to study soot size and morphology in small, laboratory-scale, surrogate nuclear waste fire plumes. The measurement technique is truly in-situ, real-time, and requires no sample extraction. It provides quantitative data for the respirable fraction of particles for rigorous health assessments. The preliminary data presented in this report, showed the potential influence of shear and condensational surface coatings on particle size and compaction level, hence

the potential influence on the respirable fraction. This is important to note since the presence of oily, high viscosity substances, such as tributyl phosphate, could impact particle growth and toxicity. Similarly, the fire environment (e.g., vorticity, turbulent kinetic energy) could also impact particle growth, respirability, and toxicity.

To err on the side of caution, many safety assessments assume the respirable fraction is 100%. This provides a conservative estimate of the potential dose to a worker exposed to smoke. Our results showed that the soot aggregates in the kerosene flame were respirable, enforcing the assumption of RF=1 made in the safety assessments. However, in some fire scenarios, such as heavily sooting fires, far from the source, the respirable fraction of particle mass would be reduced due to particle growth and coagulation. Coagulation can occur due to Brownian diffusion, thermophoretic forces, turbulence, and shear. The techniques developed in this report allow us to experimentally quantify particle size and shape at the source, and after the plume has evolved and particles have grown. These data could be used to develop and validate aerosol dynamics models aimed at predicting the evolution of particle size in high fidelity soot transport simulations. These types of simulations could be performed for both indoor and outdoor environments and would enhance the accuracy of safety assessments by predicting particle concentrations and particle size. This could be useful in defining zones of higher respirable hazards, such as within 30 meters of the fire.

Additionally, these measurements show that a range of fractal dimensions can be obtained depending on the fuel and fire conditions. The fractal dimension is a morphological parameter. Particles of different morphology behave differently aerodynamically. This affects particle transport in the environment as well as transport within the human respiratory system. The existence of primary particles (approximately 50 nm in size) within soot aggregates may also yield different toxicity based on their ability to cross into the bloodstream from within the lungs. Particle morphologies have been highlighted in this report and provide additional information to health physiologists that could enhance dose assessments.

Light scattering techniques are an enabling capability to provide tools to assess particle properties in-situ. Some data in this report may imply that light scattering signatures change upon inclusion of metallic contaminants. This could be useful in developing sensors for DOE facilities if proven to be true. Sensors of this type could be used in alarm systems and also standoff detection systems. Rigorous studies of the effects of metallic contaminants on light scattering will be the focus of future experiments.

The highlighted scientific and engineering advances could better facilitate estimating the toxicological impact of fire, and help keep members of the work force, the public, and the environment as safe as possible.

REFERENCES

[1] U. DOE, "AIRBORNE RELEASE FRACTIONS/RATES AND RESPIRABLE, FRACTIONS FOR NONREACTOR NUCLEAR FACILITIES," *CHANGE*, 1994, Accessed: May 04, 2024. [Online]. Available: https://www.dnfsb.gov/sites/default/files/Board%20Activities/Letters/2000/ltr_2000831_9411.pdf

[2] J. A. Hubbard *et al.*, "Airborne Release Fractions from Surrogate Nuclear Waste Fires Containing Lanthanide Nitrates and Depleted Uranium Nitrate in 30% Tributyl Phosphate in Kerosene," *Nucl. Technol.*, vol. 207, no. 1, pp. 103–118, Jan. 2021, doi: 10.1080/00295450.2020.1739995.

[3] J. A. Hubbard *et al.*, "Determination of Airborne Release Fractions from Solid Surrogate Nuclear Waste Fires," *Nucl. Technol.*, vol. 208, no. 1, pp. 137–153, Jan. 2022, doi: 10.1080/00295450.2021.1880255.

[4] C. R. Shaddix and T. C. Williams, "Soot: Giver and Taker of Light: The complex structure of soot greatly influences the optical effects seen in fires," *Am. Sci.*, vol. 95, no. 3, pp. 232–239, 2007.

[5] C. Sorensen and A. Chakrabarti, "The sol to gel transition in irreversible particulate systems," *Soft Matter*, vol. 7, no. 6, pp. 2284–2296, 2011.

[6] M. Y. Lin, H. M. Lindsay, D. A. Weitz, R. Klein, R. C. Ball, and P. Meakin, "Universal diffusion-limited colloid aggregation," *J. Phys. Condens. Matter*, vol. 2, no. 13, p. 3093, Apr. 1990, doi: 10.1088/0953-8984/2/13/019.

[7] M. Y. Lin, H. M. Lindsay, D. A. Weitz, R. C. Ball, R. Klein, and P. Meakin, "Universality in colloid aggregation," *Nature*, vol. 339, no. 6223, pp. 360–362, Jun. 1989, doi: 10.1038/339360a0.

[8] S. Rothenbacher, A. Messerer, and G. Kasper, "Fragmentation and bond strength of airborne diesel soot agglomerates," *Part. Fibre Toxicol.*, vol. 5, no. 1, p. 9, Jun. 2008, doi: 10.1186/1743-8977-5-9.

[9] M. Soos, A. S. Moussa, L. Ehrl, J. Sefcik, H. Wu, and M. Morbidelli, "Effect of shear rate on aggregate size and morphology investigated under turbulent conditions in stirred tank," *J. Colloid Interface Sci.*, vol. 319, no. 2, pp. 577–589, Mar. 2008, doi: 10.1016/j.jcis.2007.12.005.

[10] V. Oles, "Shear-induced aggregation and breakup of polystyrene latex particles," *J. Colloid Interface Sci.*, vol. 154, no. 2, pp. 351–358, Dec. 1992, doi: 10.1016/0021-9797(92)90149-G.

[11] T. Mokhtari, A. Chakrabarti, C. M. Sorensen, C. Cheng, and D. Vigil, "The effect of shear on colloidal aggregation and gelation studied using small-angle light scattering," *J. Colloid Interface Sci.*, vol. 327, no. 1, pp. 216–223, Nov. 2008, doi: 10.1016/j.jcis.2008.08.017.

[12] I. Colbeck, L. Appleby, E. J. Hardman, and R. M. Harrison, "The optical properties and morphology of cloud-processed carbonaceous smoke," *J. Aerosol Sci.*, vol. 21, no. 4, pp. 527–538, 1990.

[13] E. F. Mikhailov, S. S. Vlasenko, A. A. Kiselev, and T. I. Ryshkevich, "Restructuring factors of soot particles," *Izv. Atmospheric Ocean. Phys.*, vol. 34, no. 3, pp. 307–317, 1998.

[14] W. Kim, C. M. Sorensen, and A. Chakrabarti, "Universal Occurrence of Soot Superaggregates with a Fractal Dimension of 2.6 in Heavily Sooting Laminar Diffusion Flames," *Langmuir*, vol. 20, no. 10, pp. 3969–3973, May 2004, doi: 10.1021/la036085+.

[15] W. Kim, C. M. Sorensen, D. Fry, and A. Chakrabarti, "Soot aggregates, superaggregates and gel-like networks in laminar diffusion flames," *J. Aerosol Sci.*, vol. 37, no. 3, pp. 386–401, Mar. 2006, doi: 10.1016/j.jaerosci.2005.05.022.

[16] R. Dhaubhadel, F. Pierce, A. Chakrabarti, and C. M. Sorensen, "Hybrid superaggregate morphology as a result of aggregation in a cluster-dense aerosol," *Phys. Rev. E*, vol. 73, no. 1, p. 011404, Jan. 2006, doi: 10.1103/PhysRevE.73.011404.
[17] C. M. Sorensen, "Light Scattering by Fractal Aggregates: A Review," *Aerosol Sci. Technol.*, vol. 35, no. 2, pp. 648–687, Jan. 2001, doi: 10.1080/02786820117868.
[18] C. M. Sorensen, *Light Scattering and Absorption by Particles: The Q-space approach*. IOP Publishing, 2022. Accessed: Apr. 25, 2024. [Online]. Available: https://iopscience.iop.org/book/mono/978-0-7503-5157-7
[19] A. Durakovic, "Medical effects of internal contamination with actinides: further controversy on depleted uranium and radioactive warfare," *Environ. Health Prev. Med.*, vol. 21, no. 3, pp. 111–117, May 2016, doi: 10.1007/s12199-016-0524-4.
[20] A. L. Brown, F. Pierce, and E. T. Zepper, "Release of Contaminants from Burning Liquids and Solids," Sandia National Lab. (SNL-NM), Albuquerque, NM (United States), SAND2022-12448, Sep. 2022. doi: 10.2172/1888156.
[21] E. T. Zepper, A. Brown, F. Pierce, T. Voskuilen, and D. Louie, "CONTAMINATED FUEL FIRES: PARAMETRIC SENSITIVITY OF RESUSPENSION AND BOILING PARTICLE EVOLUTION.," Sandia National Lab. (SNL-NM), Albuquerque, NM (United States), SAND2016-10176C, Oct. 2016. Accessed: Mar. 21, 2024. [Online]. Available: https://www.osti.gov/biblio/1399827
[22] P. A. Bryant, *Airborne Radioactive Discharges and Human Health Effects: An introduction*. IOP Publishing, 2019. Accessed: Mar. 21, 2024. [Online]. Available: https://iopscience.iop.org/book/mono/978-0-7503-1356-8
[23] N. Kinoshita *et al.*, "Assessment of individual radionuclide distributions from the Fukushima nuclear accident covering central-east Japan," *Proc. Natl. Acad. Sci.*, vol. 108, no. 49, pp. 19526–19529, Dec. 2011, doi: 10.1073/pnas.1111724108.
[24] F.-X. Ouf *et al.*, "Airborne Release Fraction of Dissolved Materials During the Combustion of Liquids Representative of Nuclear Waste Treatment Process," *Nucl. Technol.*, vol. 209, no. 2, pp. 169–192, Feb. 2023, doi: 10.1080/00295450.2022.2129274.
[25] U. DOE, "AIRBORNE RELEASE FRACTIONS/RATES AND RESPIRABLE, FRACTIONS FOR NONREACTOR NUCLEAR FACILITIES," *CHANGE*, 1994, Accessed: May 04, 2024. [Online]. Available: https://www.dnfsb.gov/sites/default/files/Board%20Activities/Letters/2000/ltr_2000831_9411.pdf
[26] A. A. Andersen, "A Sampler for Respiratory Health Hazard Assessment," *Am. Ind. Hyg. Assoc. J.*, vol. 27, no. 2, pp. 160–165, Mar. 1966, doi: 10.1080/00028896609342810.
[27] D. M. Broday and R. Rosenzweig, "Deposition of fractal-like soot aggregates in the human respiratory tract," *J. Aerosol Sci.*, vol. 42, no. 6, pp. 372–386, Jun. 2011, doi: 10.1016/j.jaerosci.2011.03.001.
[28] J. Rissler *et al.*, "Experimental determination of deposition of diesel exhaust particles in the human respiratory tract," *J. Aerosol Sci.*, vol. 48, pp. 18–33, Jun. 2012, doi: 10.1016/j.jaerosci.2012.01.005.
[29] R. A. Guilmette, "Issues and research on the biochemistry of inhaled actinides," *J. Alloys Compd.*, vol. 271–273, pp. 66–71, Jun. 1998, doi: 10.1016/S0925-8388(98)00026-7.
[30] G. Cadelis, R. Tourres, and J. Molinie, "Short-Term Effects of the Particulate Pollutants Contained in Saharan Dust on the Visits of Children to the Emergency Department due to Asthmatic Conditions in Guadeloupe (French Archipelago of the Caribbean)," *PLoS ONE*, vol. 9, no. 3, p. e91136, Mar. 2014, doi: 10.1371/journal.pone.0091136.

[31] J. Löndahl, A. Massling, J. Pagels, E. Swietlicki, E. Vaclavik, and S. Loft, "Size-Resolved Respiratory-Tract Deposition of Fine and Ultrafine Hydrophobic and Hygroscopic Aerosol Particles During Rest and Exercise," *Inhal. Toxicol.*, vol. 19, no. 2, pp. 109–116, Jan. 2007, doi: 10.1080/08958370601051677.
[32] J. S. Brown, T. Gordon, O. Price, and B. Asgharian, "Thoracic and respirable particle definitions for human health risk assessment," *Part. Fibre Toxicol.*, vol. 10, no. 1, p. 12, 2013, doi: 10.1186/1743-8977-10-12.
[33] K. Nesmerak, "Lanthanide/Actinide Toxicity," in *Encyclopedia of Metalloproteins*, R. H. Kretsinger, V. N. Uversky, and E. A. Permyakov, Eds., New York, NY: Springer, 2013, pp. 1098–1103. doi: 10.1007/978-1-4614-1533-6_151.
[34] C. Chen, D. N. Zakharov, and A. F. Khalizov, "Drastically different restructuring of airborne and surface-anchored soot aggregates," *J. Aerosol Sci.*, vol. 168, p. 106103, Feb. 2023, doi: 10.1016/j.jaerosci.2022.106103.
[35] R. P. Bambha, M. A. Dansson, P. E. Schrader, and H. A. Michelsen, "Effects of volatile coatings and coating removal mechanisms on the morphology of graphitic soot," *Carbon*, vol. 61, pp. 80–96, Sep. 2013, doi: 10.1016/j.carbon.2013.04.070.
[36] S. R. Forrest and T. A. Witten Jr, "Long-range correlations in smoke-particle aggregates," *J. Phys. Math. Gen.*, vol. 12, no. 5, p. L109, 1979.
[37] M. Frame and A. Urry, *Fractal Worlds: Grown, Built, and Imagined*. Yale University Press, 2016.
[38] M. Y. Lin, H. M. Lindsay, D. A. Weitz, R. C. Ball, R. Klein, and P. Meakin, "Universality in colloid aggregation," *Nature*, vol. 339, no. 6223, Art. no. 6223, Jun. 1989, doi: 10.1038/339360a0.
[39] D. A. Weitz, J. S. Huang, M. Y. Lin, and J. Sung, "Limits of the Fractal Dimension for Irreversible Kinetic Aggregation of Gold Colloids," *Phys. Rev. Lett.*, vol. 54, no. 13, pp. 1416–1419, Apr. 1985, doi: 10.1103/PhysRevLett.54.1416.
[40] R. H. Ebini and C. M. Sorensen, "Light scattering studies of the sol-to-gel transition in particulate systems," *J. Colloid Interface Sci.*, vol. 556, pp. 577–583, Nov. 2019, doi: 10.1016/j.jcis.2019.08.075.
[41] M. Y. Lin, H. M. Lindsay, D. A. Weitz, R. C. Ball, R. Klein, and P. Meakin, "Universal reaction-limited colloid aggregation," *Phys. Rev. At. Mol. Opt. Phys.*, vol. 41, no. 4, pp. 2005–2020, Feb. 1990, doi: 10.1103/physreva.41.2005.
[42] D. Fry, A. Chakrabarti, W. Kim, and C. M. Sorensen, "Structural crossover in dense irreversibly aggregating particulate systems," *Phys. Rev. E*, vol. 69, no. 6, p. 061401, Jun. 2004, doi: 10.1103/PhysRevE.69.061401.
[43] W. H. Dalzell, G. C. Williams, and H. C. Hottel, "A light-scattering method for soot concentration measurements," *Combust. Flame*, vol. 14, no. 2, pp. 161–169, 1970.
[44] W. R. Heinson, A. Chakrabarti, and C. M. Sorensen, "A new parameter to describe light scattering by an arbitrary sphere," *Opt. Commun.*, vol. 356, pp. 612–615, 2015.
[45] D. Hou, D. Zong, C. S. Lindberg, M. Kraft, and X. You, "On the coagulation efficiency of carbonaceous nanoparticles," *J. Aerosol Sci.*, vol. 140, p. 105478, Feb. 2020, doi: 10.1016/j.jaerosci.2019.105478.
[46] J. Morán, C. Henry, A. Poux, and J. Yon, "Impact of the maturation process on soot particle aggregation kinetics and morphology," *Carbon*, vol. 182, pp. 837–846, Sep. 2021, doi: 10.1016/j.carbon.2021.06.085.
[47] C. M. Sorensen, J. Yon, F. Liu, J. Maughan, W. R. Heinson, and M. J. Berg, "Light scattering and absorption by fractal aggregates including soot," *J. Quant. Spectrosc. Radiat. Transf.*, vol. 217, pp. 459–473, 2018.

[48] P. Gautam, J. B. Maughan, J. Ilavsky, and C. M. Sorensen, "Light scattering study of highly absorptive, non-fractal, hematite aggregates," *J. Quant. Spectrosc. Radiat. Transf.*, vol. 246, p. 106919, May 2020, doi: 10.1016/j.jqsrt.2020.106919.
[49] H. A. Michelsen, C. Schulz, G. J. Smallwood, and S. Will, "Laser-induced incandescence: Particulate diagnostics for combustion, atmospheric, and industrial applications," *Prog. Energy Combust. Sci.*, vol. 51, pp. 2–48, Dec. 2015, doi: 10.1016/j.pecs.2015.07.001.
[50] J. C. Corbin, R. L. Modini, and M. Gysel-Beer, "Mechanisms of soot-aggregate restructuring and compaction," *Aerosol Sci. Technol.*, vol. 57, no. 2, pp. 89–111, Feb. 2023, doi: 10.1080/02786826.2022.2137385.
[51] L. Wang, D. L. Marchisio, R. D. Vigil, and R. O. Fox, "CFD simulation of aggregation and breakage processes in laminar Taylor–Couette flow," *J. Colloid Interface Sci.*, vol. 282, no. 2, pp. 380–396, Feb. 2005, doi: 10.1016/j.jcis.2004.08.127.
[52] T. Serra and X. Casamitjana, "Structure of the Aggregates During the Process of Aggregation and Breakup Under a Shear Flow," *J. Colloid Interface Sci.*, vol. 206, no. 2, pp. 505–511, Oct. 1998, doi: 10.1006/jcis.1998.5714.
[53] P. T. Spicer, W. Keller, and S. E. Pratsinis, "The Effect of Impeller Type on Floc Size and Structure during Shear-Induced Flocculation," *J. Colloid Interface Sci.*, vol. 184, no. 1, pp. 112–122, Dec. 1996, doi: 10.1006/jcis.1996.0601.
[54] S. P. Kearney and F. Pierce, "Evidence of soot superaggregates in a turbulent pool fire," *Combust. Flame*, vol. 159, no. 10, pp. 3191–3198, Oct. 2012, doi: 10.1016/j.combustflame.2012.04.011.
[55] R. K. Chakrabarty *et al.*, "Soot superaggregates from flaming wildfires and their direct radiative forcing," *Sci. Rep.*, vol. 4, no. 1, Art. no. 1, Jul. 2014, doi: 10.1038/srep05508.
[56] W. R. Heinson, Y. W. Heinson, P. Liu, and R. K. Chakrabarty, "Breakdown of fractal dimension invariance in high monomer-volume-fraction aerosol gels," *Aerosol Sci. Technol.*, vol. 52, no. 9, pp. 953–956, Sep. 2018, doi: 10.1080/02786826.2018.1492086.
[57] KoHse-HoingHaus, *Applied Combustion Diagnostics*. CRC Press, 2002.
[58] T. Mouton, X. Mercier, M. Wartel, N. Lamoureux, and P. Desgroux, "Laser-induced incandescence technique to identify soot nucleation and very small particles in low-pressure methane flames," *Appl. Phys. B*, vol. 112, no. 3, pp. 369–379, Sep. 2013, doi: 10.1007/s00340-013-5446-x.
[59] P. N. Langenkamp, J. A. van Oijen, H. B. Levinsky, and A. V. Mokhov, "Growth of Soot Volume Fraction and Aggregate Size in 1D Premixed C_2H_4/Air Flames Studied by Laser-Induced Incandescence and Angle-Dependent Light Scattering," *J. Combust.*, vol. 2018, p. e2308419, Oct. 2018, doi: 10.1155/2018/2308419.
[60] K. Frederickson, S. P. Kearney, and T. W. Grasser, "Laser-induced incandescence measurements of soot in turbulent pool fires," *Appl. Opt.*, vol. 50, no. 4, pp. A49–A59, Feb. 2011, doi: 10.1364/AO.50.000A49.
[61] P. Desgroux, X. Mercier, B. Lefort, R. Lemaire, E. Therssen, and J. F. Pauwels, "Soot volume fraction measurement in low-pressure methane flames by combining laser-induced incandescence and cavity ring-down spectroscopy: Effect of pressure on soot formation," *Combust. Flame*, vol. 155, no. 1, pp. 289–301, Oct. 2008, doi: 10.1016/j.combustflame.2008.05.016.
[62] H. Oltmann, J. Reimann, and S. Will, "Wide-angle light scattering (WALS) for soot aggregate characterization," *Combust. Flame*, vol. 157, no. 3, pp. 516–522, Mar. 2010, doi: 10.1016/j.combustflame.2009.10.011.

[63] H. Oltmann, J. Reimann, and S. Will, "Single-shot measurement of soot aggregate sizes by wide-angle light scattering (WALS)," *Appl. Phys. B*, vol. 106, no. 1, pp. 171–183, Jan. 2012, doi: 10.1007/s00340-011-4781-z.
[64] S. Gangopadhyay, I. Elminyawi, and C. M. Sorensen, "Optical structure factor measurements of soot particles in a premixed flame," *Appl. Opt.*, vol. 30, no. 33, pp. 4859–4864, 1991.
[65] E. J. Lee and H. J. Shin, "Smoke characteristics of kerosene pool fires," in *Proceedings of Council on Tall Buildings and Urban Habitat (CTUBH) Conference, Seoul, Korea*, 2004, pp. 950–956. Accessed: Mar. 20, 2024. [Online]. Available: https://global.ctbuh.org/resources/papers/download/1745-smoke-characteristics-in-kerosene-pool-fires.pdf
[66] R. K. Chakrabarty, H. Moosmüller, M. A. Garro, and C. B. Stipe, "Observation of Superaggregates from a Reversed Gravity Low-Sooting Flame," *Aerosol Sci. Technol.*, vol. 46, no. 1, pp. i–iii, Jan. 2012, doi: 10.1080/02786826.2011.608389.
[67] P. Gautam and C. M. Sorensen, "A wide range (0.32°–177.6°), multi-angle light scattering setup and concomitant analysis method," *Rev. Sci. Instrum.*, vol. 92, no. 11, 2021, Accessed: Jul. 09, 2024. [Online]. Available: https://pubs.aip.org/aip/rsi/article/92/11/113105/596134
[68] P. Gautam, "Light scattering study of irregular particles with arbitrary size, shape, and complex refractive index," Jul. 2022, Accessed: May 07, 2024. [Online]. Available: https://hdl.handle.net/2097/42344
[69] Y. W. Heinson, *Light scattering studies of irregularly shaped particles*. Kansas State University, 2016. Accessed: May 07, 2024. [Online]. Available: https://search.proquest.com/openview/64bcd2f40e4e8b8a371eddfd14134141/1?pq-origsite=gscholar&cbl=18750
[70] F. Ferri, "Use of a charge coupled device camera for low-angle elastic light scattering," *Rev. Sci. Instrum.*, vol. 68, no. 6, pp. 2265–2274, 1997.
[71] "Seasonal maximum and minimum temperature and relative humidity data for...," ResearchGate. Accessed: May 08, 2024. [Online]. Available: https://www.researchgate.net/figure/Seasonal-maximum-and-minimum-temperature-and-relative-humidity-data-for-Manhattan-Kansas_tbl1_349430556

DISTRIBUTION

Email—Internal

Name	Org.	Sandia Email Address
Raiya Ebini	1516	rhebini@sandia.gov
Flint Pierce	1514	fpierce@sandia.gov
Ben Zeidman	0531	bdzeidm@sandia.gov
Josh Hubbard	1516	jahubba@sandia.gov
Dora Wiemann	6792	dkwiema@sandia.gov
Taylor Settecerri	6633	tsettec@sandia.gov
Alex Brown	1532	albrown@sandia.gov
Technical Library	1911	sanddocs@sandia.gov

Email—External

Name	Company Email Address	Company Name
Christopher Sorensen	sor@phys.ksu.edu	Kansas State University

Sandia National Laboratories

Sandia National Laboratories is a multimission laboratory managed and operated by National Technology & Engineering Solutions of Sandia LLC, a wholly owned subsidiary of Honeywell International Inc. for the U.S. Department of Energy's National Nuclear Security Administration under contract DE-NA0003525.